JOURNAL OF AIRCRAFT
Vol. 47, No. 5, September–October 2010

Theoretical Framework for the Simulation of Transport Aircraft Flight

Antonio Filippone*
University of Manchester, Manchester, England M60 1QD, United Kingdom

DOI: 10.2514/1.C000252

This contribution presents a novel simulation theory for a complete fixed-wing aircraft. Novel methods are presented for flight mechanics (fuel planning), turbofan engine simulation (indirect and inverse mode), thermophysics integration (tire temperature on the ground and fuel temperature in-flight) and aircraft noise. At the fundamental level, the framework presented addresses a shortfall in multidisciplinary integration in aircraft flight, including economic operations, preliminary design and environmental emissions. The models introduced are based on first principles, supplied with semiempirical correlations, when necessary. Validation strategies are introduced for component-level analysis and system integration. Results are presented for geometry models, specific air range and optimal cruise conditions, payload-range performance, fuel temperature of a wing tank, tire heating during normal takeoff, aircraft propulsive (jet/nozzle), and nonpropulsive (landing gear) noise. Selected results are shown for the Boeing B777-300 and the Airbus A380-861.

Nomenclature

A	=	wing area
b_t	=	thrust arm
b_{tank}	=	wing tank span
C_a	=	aerodynamic coefficient
C_{Lo}	=	wing's zero-incidence lift coefficient
$C_{L\alpha}$	=	wing's lift-curve slope
C_{L_ξ}	=	V-tail-rudder's lift curve slope
C_p	=	heat transfer coefficient at constant pressure
D	=	drag force
d_w	=	wheel diameter
E	=	energy
$\mathcal{E}$	=	engine state parameter
F	=	normal force on tire
F_N	=	net thrust
f	=	frequency
g	=	acceleration of gravity
$\mathcal{H}$	=	mechanical hysteresis
h	=	flight altitude
h_c	=	convective heat transfer coefficient
k_c	=	thermal conductivity
l_c	=	length of tire-road contact
L	=	lift force
$\mathcal{L}$	=	characteristic length
M	=	Mach number; moment
M_{ow}	=	wing pitching moment
m_f	=	fuel mass
n	=	iteration count
Nu	=	Nusselt number
p	=	pressure
$\boldsymbol{P}$	=	operational rating
Q	=	heat transfer
$\bar{Q}$	=	heat transfer between liquid/vapor fuel
Re	=	Reynolds number
Re_r	=	rotating-flow Reynolds number
$\boldsymbol{r}$	=	position vector
$\mathcal{S}$	=	generic surface
S	=	convective surface
$\bar{S}$	=	surface shared by liquid and vapor fuel
T	=	net thrust
$\mathcal{T}$	=	temperature
t	=	time
V	=	volume
V_{LO}	=	liftoff speed
V_{MCG}	=	minimum control speed in ground
v_c	=	climb rate
w_b	=	wheel base
W	=	weight
$\mathcal{W}$	=	work done
$\mathcal{W}_1$	=	work done during full tire rotation
X_{req}	=	required range
X_1	=	first estimate of aircraft range
x	=	flight distance
x_c, x_d	=	enroute climb and descent distance
x_{vt}	=	distance between rudder lift and main landing gear
$\boldsymbol{x}$	=	aircraft state parameters
$\boldsymbol{x}_o$	=	position of noise receiver
$\boldsymbol{X}$	=	aircraft position
$\boldsymbol{y}(.)$	=	flight state parameters
Y_n	=	side force on nose wheels
z_t	=	vertical distance between net thrust and c.g.
$\boldsymbol{z}(.)$	=	vector of atmospheric parameters

Greek Symbols

α	=	angle of attack
α_e	=	effective angle of attack
α_{ns}	=	angle of attack due to relaxation of nose landing gear
α_o	=	airplane attitude on the ground
γ	=	flight-path angle
Δz	=	average vertical tire deformation
θ	=	polar emission angle
δ_f	=	flap deflection
δ_t	=	tire's vertical deflection
μ	=	dynamic viscosity
μ_r	=	rolling resistance coefficient
μ_{rs}	=	lateral rolling coefficient
ξ	=	rudder deflection
Π	=	throttle setting

Received 11 January 2010; revision received 29 April 2010; accepted for publication 30 April 2010.

*School of Mechanical, Aerospace and Civil Engineering. George Begg Building, P.O. Box 88; a.filippone@manchester.ac.uk. Senior Member AIAA.

ρ	=	density
τ	=	time constant
ω	=	rotational velocity

Subscripts and Superscripts

$[.]_c$	=	climb
$[.]_d$	=	descent
$[.]_f$	=	fuel
$[.]_g$	=	gas or ground effect
$[.]_m$	=	main landing gear
$[.]_n$	=	nose landing gear
$[.]_r$	=	roadway
$[.]_{\text{res}}$	=	reserve
$[.]_t$	=	tire
$[.]_{\text{vt}}$	=	vertical tail
$[.]^*$	=	estimated parameter

I. Introduction

WE ADDRESS the use of comprehensive computer models for fixed-wing aircraft. These models, properly formulated from a mathematical point of view, and efficiently programmed, can be used for a variety of engineering tasks; these tasks range from aircraft design to the prediction of environmental effects (exhaust emissions and noise), and include operational aspects at all levels. Comprehensive flight models fall in one of these categories: flight dynamics, flight simulation, aircraft design, operational performance, and stability. This contribution focuses on the latter aspect of aircraft flight.

Most of the current research activities are based on specific models for aerodynamics, propulsion, or noise. A combination of these and other disciplines remains largely unexplored. Yet, there is considerable potential for flight analysis at several levels, as demonstrated by an increasing interest in multidisciplinary optimization; this application requires high-fidelity models for the various aircraft before any optimization strategy [1]. A flight optimization system called FLOPS was developed in the 1980s [2] to deal with detailed performance during preliminary design. FLOPS used a similar modular approach, but relied on statistics and other low-level simplifications, such as energy methods for climb optimization.

The step toward this multidisciplinary simulation platform faces a number of difficulties. First, there is the problem of extracting relevant information for an existing airplane. Second, one must decide how much physics to introduce in the computer model; finally, once the models become available, there is the problem of testing and validation, because of the scarcity of reliable data. Some of these difficulties could be overcome if flight data recorder (FDR) could be made public. Modern FDR store several hundred flight parameters, and are the most comprehensive source of data for comparison with flight simulation data. In the absence of such information, the validation of the simulation models must rely on a set of cross-analysis that include aerodynamics, propulsion system, airframe-engine integration, economic cruise Mach numbers, payload-range charts and a number of sensitivity analysis. Thus, the development of comprehensive models must be done around an environment with uncertain data.

The first step is to establish a multidisciplinary theoretical framework that is balanced and accurate. This framework includes the geometrical definition of the airplane, its operational state and the environment in which it operates. These three aspects of the model are the foundation of a set of multidisciplinary packs.

When building top-level models, such as aerothermodynamics and system's dynamics, it is important that the main aspects of the physics are included; a decision of what to set aside depends largely on experience, on limitations to computational complexity, and on the techniques that are available for validation and testing.

Previous publications have addressed some aspects of aircraft flight simulation. In particular, [3] presented a full review of the state-of-the-art in comprehensive flight mechanics models. We refer to this paper for a review of the subject. Reference [4] has addressed flight control and optimization strategies for a continuous steep final approach. Reference [5] addressed a parametric analysis for aircraft emissions. In this paper further advancements are shown in selected areas, along with a generalization of some aspects of the computer code. Hence the concept of flight performance is extended to include several new multiphysics aspects, with special attention to accuracy and reliability. Figure 1 shows the conceptual flowchart used in the mathematical modelling. The computer code is called FLIGHT. On each deck, there is a coherent set of data and models. For example, in the input deck there are data for the reconstruction of the airplane (whose physical breakdown is shown in Fig. 2), propulsion data,

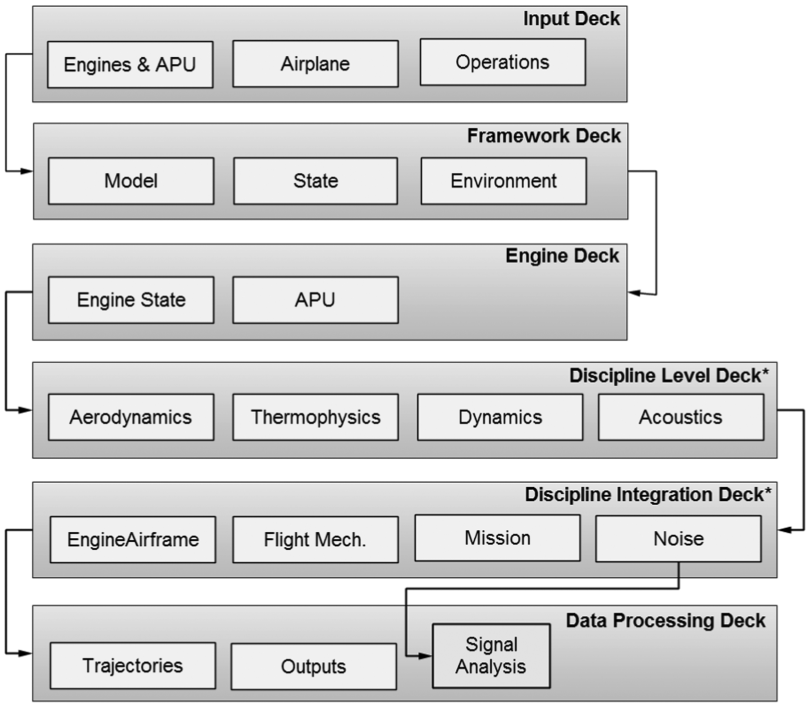

Fig. 1 Multiphysics implementation of flight performance; [*] denotes selected disciplines.

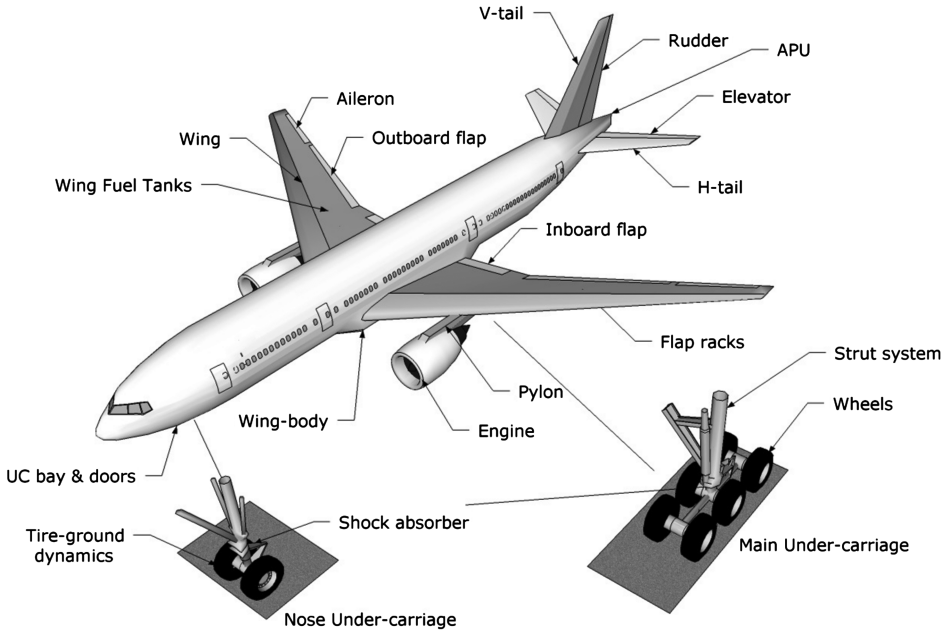

Fig. 2 Assembly of aircraft systems for present mathematical model.

limitations and operational requirements. In the following sections we describe the framework for analysis, an intermediate deck for the propulsion system, some multidisciplinary developments and selected strategies at the integration deck.

II. Theoretical Framework

The top-level theoretical framework deals with the airplane shape, state and outside environment. To start with, the airplane is based on the following concept:

$$\texttt{Model} = \boldsymbol{f}[\boldsymbol{x}(t)] \tag{1}$$

where $\boldsymbol{x} = \{x_1, x_2, \cdots x_n\}$ are aircraft state parameters, some of which depend on the time t. For example, a subset of the parameters $\boldsymbol{x}_i$ may denote the position of the control surfaces and the undercarriage. The state parameters are divided into separate categories: 1) geometry (control points, shape parameters, angle settings, etc.), 2) assembly (subsystems and complete model), and 3) systems (power-plant, fuel systems, auxiliary power units (APU), etc.).

There are several ways in which the functional relationship Eq. (1) can be constructed. In this context we have used an approach that is based of a database of control points, and on geometrical rules. Each aircraft system (or element) is assigned an identity card, a sequence of control parameters, and a series of rules to manipulate the control parameters. The rules include a local and a global reference system. The reconstruction of the system (or element) is done through the information read from the card and the reconstruction algorithms that have been programmed for that particular case.

This method could be generalized further, to include the determination of Eq. (1) via a recognized computer-aided design standard, such as DXF and IGES. It is not unusual that key elements (particularly those related to engines and control surfaces) are missing. These are replaced with statistical correlation of available data.

The state of the airplane is defined by the formal relationship is required; this is

$$\texttt{State} = \boldsymbol{f}[\boldsymbol{y}(t)] \tag{2}$$

where $\boldsymbol{y} = \{y_1, y_2, \cdot, y_m\}$ are flight state parameters. In most cases, the parameters are time-dependent and indicate deployment and retraction of landing gear, deployment and retraction of individual high-lift systems, individual flight controls and so forth. The state parameters can be further divided into the following categories:

1) *Structures*: weight components loads, position of the c.g., moments of inertia.

2) *Propulsion*: aerothermodynamic parameters of the engine.

3) *Flight mechanics*: velocity vector (heading, air speed, climb rate) and attitude angles.

Clearly, there must be a further relationship between Eqs. (1) and (2); the latter equation requires some control inputs.

The aircraft operates in the atmosphere, for which a formal relationship is

$$\texttt{Atmosphere} = \boldsymbol{f}[\boldsymbol{z}(t)] \tag{3}$$

where $\boldsymbol{z} = \{z_1, z_2, \cdot, \}$ are local atmospheric parameters such as temperature, pressure, density, relative humidity, viscosity, turbulence level, wind speed and direction, and other external factors, such as airfield conditions. At the basic level, we use the standard atmosphere to calculate the properties of dry air. Turbulence data are used for the aerodynamics, including boundary layer transition on the wings, and noise generated by the acoustic scattering of the boundary layer at the trailing edge of the lifting surfaces. Relative humidity data are used for calculation of contrail factors, for contrail avoidance strategy, trajectory optimization, noise propagation and absorption.

The engine is simulated in reverse, as discussed in Sec III, according to the formal relationship

$$\texttt{EngineState} = \boldsymbol{f}[T(t)] \tag{4}$$

where T denotes the required net thrust (a quantity that can be replaced by the required power). This function is described next.

III. Propulsion System

The physical model for the propulsion system is a continuous mass flow engine, simulated with a steady-state one-dimensional flow approximation. The simulation environment of the airplane often requires the determination of the engine state from a required thrust or power output. Thus, the engine must be simulated in *reverse*. Before doing so, a determination of the normal state of operation is required to identify the critical engine parameters. This is done at takeoff thrust, under static sea level normal conditions. Under this condition, we are able to determine critical data from the type certificate: nominal rpm (for dual spool engines: `N1`, `N2`); limit temperature at designated sections of the engine (normally, a certain

Table 1 Engine parameters used for flight analysis

Symbol	Description
W1	Mass flow rate
N%1	Low pressure rotor rpm, %
TT3	Combustor inlet temperature
PT3	HP Compressor pressure, exit
TT4	Exit combustor temperature
Wf6	Fuel flow rate
TT5	Power turbine temperature
FN	Net thrust
TSFC	Specific fuel consumption
TS9	Total static nozzle temperature
PS9	Total static nozzle pressure
M9	Nozzle Mach number (core)
TT2.1	Exit fan temperature (core side)
TT2.2	Exit fan temperature (bypass side)
N%2	High pressure rotor rpm, %
WC2.5	Core mass flow rate
TT2.5	LP compressor exit temperature
PT2.5	LP compressor exit pressure
TT14	Bypass flow temperature, exit
PT14	Bypass flow total pressure, exit

stage in the turbine section); the limit exhaust gas temperature TS9; the corresponding engine thrust FN.

The design parameters are: takeoff thrust, mass flow rate W1, fuel flow rate Wf6, power turbine inlet temperature TT5 (or LPT temperature TT4.5, or static exhaust gas temperature TS9), power shaft rpm in percent N%1. These parameters are also listed in Table 1. Let us assume that we wish to find the operation point of the engine by using the TT5 limit temperature. The formal relationship that has to be found is

$$\mathtt{DesignPoint} = f(\mathtt{FN}, \mathtt{W1}, \mathtt{Wf6}, \mathtt{TT5}, \mathtt{N\%1}) \tag{5}$$

Through a parametric analysis, it is possible to estimate the design point. We constrain the parameters N%1 and TT5. We perform a two-dimensional search on the plane W1-Wf6, which leads to a variable FN and variable TT5. The design point is found where the value of the limit FN-curve intersects the limit TT5-curve. At this point, the engine will have a unique value of W1 and Wf6. This is not a guarantee that the estimated point is indeed correct, although the solution is unique for a realistic thermodynamic model. This step is one of the most important procedures of the full engine-airframe integration.

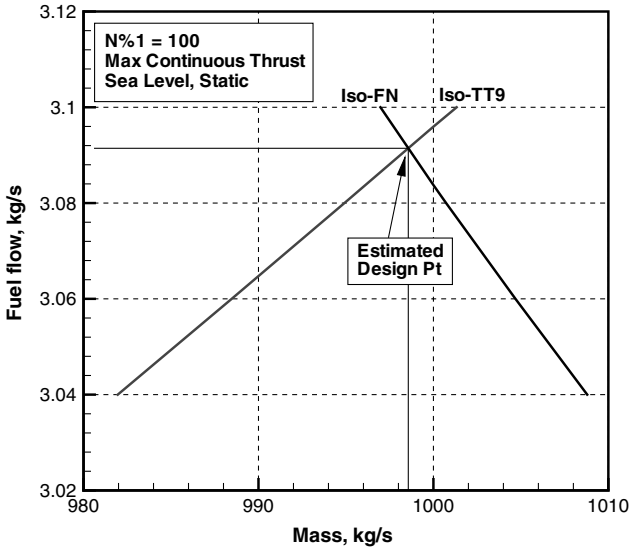

Fig. 3 Estimation of design point for the GP-7270 engine; labeled points denote net thrust.

The result of this analysis is shown in Fig. 3 for the turbofan engine GP-7270, that powers the Airbus A380-861. For this engine, the turbine temperatures are not given. However, the total limit EGT is provided. Thus, in this case, the design point is given by the intersection of the iso-FN line and the iso-TT9 line at the specified operating conditions. The corresponding TSFC is calculated from $f_j = \dot{m}_f/T = \mathtt{Wf6}/\mathtt{FN}$.

The flight envelope is defined by a range of Mach numbers, flight altitudes, atmospheric temperatures below and above the standard day. Within these limits, the engine can assume a large number of states, defined by the fuel flow. The latter parameter can be associated to a throttle setting. For convenience, engine envelopes are generated a priori by using the gas turbine program (GSP) [6] and used as a database. The reason for this strategy is that the program generally requires the determination of the engine state for a given net thrust and flight condition (Mach, altitude, outside air temperature). In Fig. 4, this requirement is indicated by the dashed line from the thrust to the fuel feed box. Vice versa, from the point of view of the engine, the engine state would be defined by a fuel flow or throttle position. A complex high-order interpolation (cubic spline) through a four-dimensional space is used to define the engine state. If $\mathcal{E}$ is an engine parameter, its dependence from the operational conditions is

$$\mathcal{E} = f(\text{rate}, \boldsymbol{P}, \Pi) \tag{6}$$

where "rate" indicates the engine operational rating (takeoff, maximum continuous thrust); $\boldsymbol{P} = \{\mathrm{d}\mathcal{T}, M, h\}$ denotes the vector of operational parameters; $\mathrm{d}\mathcal{T}$ is the temperature difference from the standard day, M is the flight Mach number, h is the flight altitude and Π is the throttle. Then we use a high-order multidimensional interpolation of the matrix at the point defined by the vector $\boldsymbol{P}$. We use the functional $\mathcal{E}_1 = f_1(\Pi)$ to define all the engine states at the given rating and operational point. When $\Pi = 1$, the engine is at its operational limit, that must be defined. The steady-state engine envelope is calculated by using a combination of limit gas-generator turbine temperature (TT5) and rotational speed in percent (N%1), as indicated by the named circles in Fig. 4. These data are available from the engine type-certificate.

Twenty engine parameters are used for integration the aircraft flight; these are divided into two categories: engine parameters for flight mechanics simulation and parameters for engine noise simulation. This split of parameters gives better memory management and faster computing. The aircraft noise module requires at least the temperatures across the parts of the engine, the pressure rise or loss through all the stages, and the aerothermodynamic properties of the jet at the nozzle. The list of engine parameters used in the mathematical model of the airplane are listed in Table 1.

In addition to the state of the engine, it is possible to calculate the instantaneous combustion emission characteristics. This is currently done by using the International Civil Aviation Organization database [7], with a provision for the actual state. On output, the model

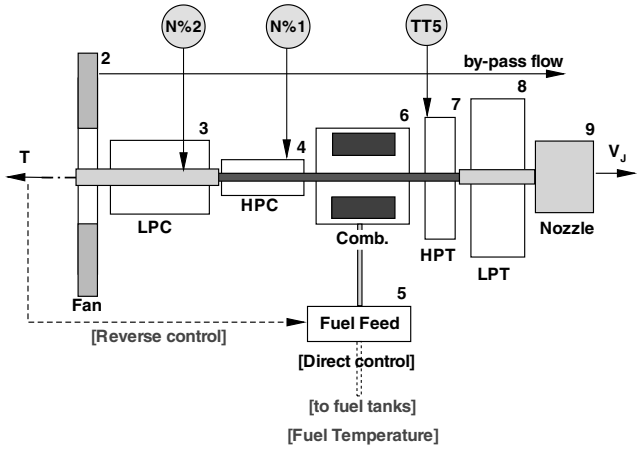

Fig. 4 Engine model and related systems and controls.

provides rates of CO and NO_x that can be used for landing–takeoff (LTO) emission analysis.

There is no provision for analysis of the APU, because no engineering data are generally available to perform a computer simulation. Our model is limited to an average fuel flow in the environmental conditioning mode. The APU fuel flow is important from the point of view of the mission planning and is added to the total count of fuel consumption. For example, the A380 APU burns up to 470 kg/h at full power and requires a few tons of fuel over a long-haul flight.

IV. Aerodynamic Models

The aerodynamic model has been published previously [3]. In brief, it consists of a combination of theories that address all the drag components of the airplane. If C_a denotes an aerodynamic coefficient or its derivative, then

$$C_a = \boldsymbol{f}(\texttt{State}, \texttt{Atmosphere}) \tag{7}$$

The coefficient is the result of the contribution from the various subsystems of the airplane, following the principle of independent components.

The induced drag is calculated from a lifting surface code, that is also used for the determination of the aerodynamic derivatives of the lifting surfaces (wing, horizontal tail, and vertical fin). The derivatives are an integral part of the comprehensive model, because they are at the basis of static stability analysis, both on the ground and in the air. The assembly and disassembly of the aircraft systems is shown in Fig. 2; this figure also lists the main subsystems modeled by the FLIGHT program.

The profile drag is calculated with a combination of laminar and turbulent flow theories, including the Eckert equilibrium temperature model (as shown by Nielsen [8]), the van Driest theory for turbulent flow (as shown by Hopkins [9] and Hopkins and Inouye [10]), the turbulence transition model of Blumer and van Driest on a flat plate [11], and surface curvature corrections (following Hoerner [12]), on the basis of the local relative thickness. The lifting surfaces are divided into strips; each strip is associated to an equivalent flat plate, and the contributions from all strips are summed up to provide the integral profile drag.

For the fuselage, the nose cone theory of White [13] and the tail drag model of Engineering Sciences Data Unit (ESDU) [14] are implemented, to account for the integral effects of the fore and aft fuselage. The wave drag is calculated for all the lifting surfaces with a modified version of the model by Malone and Mason [15], and further discussed in [3] by using an appropriate value of the effects of the aerodynamic lift on the divergence Mach number. This method is coupled with an empirical relationship for the critical Mach number. In general, there is a wave drag arising from the wing and the horizontal tail. The divergence Mach number of the vertical stabilizer is considerably larger than the operating Mach number, and it does not contribute to the wave drag.

The method presented has been validated for a number of practical cases at cruise conditions, including the Boeing 747-100, the Boeing 777 and the DLR F4 wing-body and F6 wing-body-nacelle combination [3] with reasonable accuracy.

For other phases of flight additional aerodynamic theories are required for both lift and drag. The high-lift systems are modeled with ESDU [16]; an implementation of this method provides the lift, maximum lift and the corresponding drag corresponding to a deflection of a combination of slats and flaps. Although these models do not have a provision for flow physics, they provide a rapid estimation of the change in aerodynamic parameters, as long as the parametric space of the airplane is within reasonable bounds.

Another item of interest is the drag rise due to deployment of undercarriage. For this purpose, a modification of the ESDU method [17] is used. The implementation followed in this study includes the disassembly of the undercarriage units into wheels, strut system, bay and bay doors, followed by an assembly of the drag components for each components [3]. In particular, there is a provision to account for various combinations of wheels. The effect of the cavity drag is extrapolated from time-averaged experimental data.

As far as the high-lift configuration is concerned, the aerodynamic forces are calculated through the functionals

$$\text{Lift} = f(\texttt{FlightControls}, \text{TAS}, h, \alpha, \texttt{Atmosphere}) \tag{8}$$

$$\text{Drag} = f(\texttt{FlightControls}, \text{TAS}, h, \alpha, \texttt{Atmosphere}) \tag{9}$$

where $\texttt{FlightControls}(t)$ denotes the operator

$$\texttt{FlightControls}(t) = (\texttt{Flaps}, \texttt{LGear}) \tag{10}$$

This is an impulsive switch of either flight control. If the `Lgear` is switched off at time $t = t_1$, the calculation of the undercarriage drag is omitted. If the `Flaps` is switched off at time $t = t_2$, the calculation of the lift and drag of the high-lift system is omitted. However, the flap control contains the deflection angle, which can be changed. The impulsive change in the aerodynamics is justified by the fact that the time steps generally used in this type of performance analysis are too large compared with the aerodynamic transients. In any case, the aerodynamic theory used is steady state, and it would not be possible to capture these transients.

For the calculation of the aerodynamic forces, the effective wing angle of attack is the result of several contributions: 1) pitch attitude of the airplane α_o (nose down during the ground roll), 2) the mean inclination of the reference wing on the longitudinal axis of the airplane $\bar{\alpha}$, 3) the direction of the incoming velocity (parallel to the roadway during the ground run), 4) the change in effective inflow due to ground effect α_g, and 5) the change in inflow angle due to relaxation of nose landing gear shock absorbers α_{ns}. For the latter contribution, we have added a one-dimensional visco-elastic model of the shock absorber. The remaining contributions are calculated from the flight mechanics, except the ground effect, which is calculated a priori with a vortex lattice method as a function of both lift coefficient and ground clearance. The effects contribute linearly to the effective inflow equation

$$\alpha_e = \alpha_o + \bar{\alpha} + \gamma + \alpha_g + \Delta\alpha_{\text{ns}} \tag{11}$$

For reference, the ground contribution can be as large as 1°; by contrast, the shock absorber is 2 orders of magnitude lower. For example, the lift coefficient is calculated from

$$C_L = C_{Lo} + \Delta C_L(\delta_f) + C_{L_\alpha}\alpha_e \tag{12}$$

that includes the effects of flap deflection δ_f on the zero-incidence lift C_{Lo}.

Finally, there is a number of second-order corrections, including ground effects due to the wing proximity to the ground during all phases of roll, effects of aerodynamic deterioration (gaps and surface roughness) and the trim drag (discussed further in Sec. VI). It is important to note that, while the aerodynamic theory used is either low-order or semiempirical, more refined models, such as those based on computational fluid dynamics (CFD) [18], cannot be used in the framework established by the diagram of Fig. 1. Furthermore, any improvement in aerodynamic prediction arising from these models comes to a halt when a full integration with the engine model is required: the accuracy of the overall method is determined by the inaccuracy of just one element.

V. Thermophysics Models

We now move one step up, and consider the integration of some disciplines (Integration Deck in Fig. 1). We present the case of thermophysics, and the way it is connected with the aircraft flight or ground operations. The thermophysics discussed here deals with the simulation of the fuel temperature and the tire temperature at takeoff and landing. Both models rely on the lumped mass concept, whereby the system is reduced to a an isotropic mass, either a fluid or a solid one. These models share several characteristics. The use of the lumped mass approximation is appropriate in the context of

comprehensive aircraft performance, although at a more detailed level it would be appropriate to consider the multidimensional aspects of this thermophysics. The models rely on systems of ordinary differential equations that can be synchronized with the flight mechanics model. Fuel temperature problems are associated to cruise in very cold atmospheres. Tire heating problems cause performance limitations at heavy takeoff weights and rejected takeoff.

A. Fuel Temperature

The fuel temperature is modeled through the functional

$$T_f = f(t, \mathrm{TAT}, \mathrm{SAT}, \dot{m}_f, \dot{Q}, \mathtt{Rule}, \mathcal{S}) \tag{13}$$

where TAT and SAT denote the total air temperature and the static air temperature, respectively; $\dot{Q}$ is the heat transfer rate to the fuel through external systems, `Rule` is the fuel use rule; $\mathcal{S}$ is a geometrical operator, as discussed next. The fuel use rule depends on the aircraft and various flight procedures. For example, the center tanks may be used first, in which case, the fuel level of the wing tanks remains constant for a finite amount of time. In other cases, fuel is pumped from one tank to another for weight management purposes; therefore, the fuel level does not go down when fuel is burned. All these procedures ultimately affect the fuel temperature. The synchronization of Eq. (13) with the flight mechanics is done via the TAT, SAT, and $\dot{m}_f$.

Assuming that the essential geometrical information is in place, it is possible to calculate the exact volume of the geometry and the contact surface for any level of the fuel between a minimum and a maximum. In practice, it is possible to define a numerical function

$$\mathcal{S} = f(V) \tag{14}$$

that gives the geometrical parameter $\mathcal{S}$ as a function of the fuel volume. Specifically, the parameter $\mathcal{S}$ refers to the fuel tank wetted area, the free surface area, and the normalized fuel level (zero indicates empty tank). Equation (14) is calculated numerically from the construction of the wing tanks from the airplane database. An example is shown in Fig. 5, that displays the fuel level and the liquid fuel contact area for the wing tanks of the Boeing B-777-300 airplane model. Irregularities, due to interpolation error, may appear, including a fuel level not reaching unity with a full tank or unrealistic fuel levels for nearly empty tanks.

With reference to Fig. 5, if the fuel level is 70%, the fuel volume is about 40% of the tank's capacity (point A) and the fuel tank contact area is about 87% of the total area enveloped by the tank (point B).

The heat transfer from the fuel to the outer system takes place through contact. The heat transfer problem is defined by a system of 12 differential equations

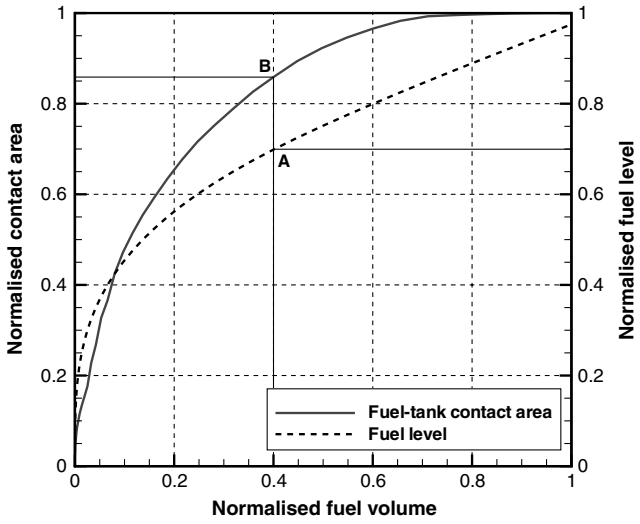

Fig. 5 Geometrical characteristics of a wing tank.

$$\frac{\mathrm{d}\boldsymbol{Y}}{\mathrm{d}t} = \boldsymbol{f}(\mathcal{T}) \tag{15}$$

where the vector of unknowns $\boldsymbol{Y}$ is

$$\boldsymbol{Y} = \{[S, Q, V_f, \mathcal{T}_f, \rho_f]_{\mathrm{liq}}, [S, Q, V_f, \mathcal{T}_f, \rho_f]_{\mathrm{vap}}, \bar{S}, \bar{Q}\} \tag{16}$$

The vector of unknown is made of a subvector $[.]_{\mathrm{liq}}$ for heat transfer between the liquid fuel and the tanks, a subvector $[.]_{\mathrm{vap}}$ for the heat transfer between the vapor phase and the tanks, the free surface $\bar{S}$ (shared by the two phases) and the corresponding heat transfer rate, $\pm\bar{Q}$.

It can be observed that some of these equations are straightforward. For example, the change in liquid fuel contact is equal to the opposite change in vapor fuel contact. The fuel vapor is described with the non linear gas equation of Peng and Robinson [19]. The thermophysical properties of the fuel vapor are inferred from Faith et al. [20], and extrapolated whenever data are not available.

To calculate the heat transfer rates, we need to estimate the transfer coefficients. This is done through the Nusselt number

$$Nu = \frac{h_c \mathcal{L}}{k} \tag{17}$$

that is the ratio between the convective heat transfer and the conduction heat transfer through a solid surface. In Eq. (17), $\mathcal{L}$ represents the characteristic length of the process, which is in this case is taken as $\mathcal{L} \simeq S/b_{\mathrm{tank}}$, i.e., the ratio between the wetted area and the spanwise extent of the tank b_{tank}. Thus, if a suitable expression for the Nusselt number is found, then the convective heat transfer to be used in the differential equations is calculated from Eq. (17).

If we neglect the heat transfer between the liquid and vapor through the free surface, four ODEs in the system Eq. (40) become redundant. A combination of the remaining equations leads to a simple equation for the liquid fuel temperature

$$\frac{\mathrm{d}\mathcal{T}_f}{\mathrm{d}t} = \frac{h_c \mathcal{S}}{C_p m_f}(\mathcal{T}_f - \mathcal{T}) \tag{18}$$

where in this case $\mathcal{T}$ is the tank temperature. The effect of fuel level is implicit in the factor $\mathcal{S}$. A similar combination for the vapor fuel, leads to an equivalent equation for the vapor temperature. The factor

$$\tau = \frac{C_p m_f}{h_c S} \tag{19}$$

represents a time constant in similar thermodynamic problems. The higher this factor, the more slowly the fuel responds to changes in temperature. A too rapid fuel cooling is not a good thing; therefore, one may want to find ways to increase the time constant. From the definition of Eq. (19), it can be gleaned that for a given fuel mass, τ increases as the contact surface decreases. However, it is also clear that τ cannot be constant, because fuel flows in or out of the tank, the contact surface changes, and the heat transfer coefficient changes as a result of variable outside conditions.

From heat transfer textbooks [21] we can find various expressions for the Nusselt numbers, depending on whether the flow is laminar, transitional or turbulent; specific research addresses heat transfer rates in jet fuels. We use equations for a natural convection problem from a warm lower surface and a cold upper surface [21]; hence, with some extrapolation, we apply this model to the cooling of the liquid and vapor fuel. For the calculation of the Nusselt numbers we need a reference length.

The total heat transfer coefficient h_c depends on the tank's material construction and it requires the determination of the total transmittance of the tank system. The heat transfer is dominated by the conduction-convection on the air side, with some contribution from the fuel side. A typical value of thermal conductivity for aluminum is 220 to 250 $\mathrm{W/m^2\,K}$, while the convective heat transfer of the air is between 10 and 100 $\mathrm{W/m^2\,K}$. In this context, the fuel will cool more rapidly when the fuel mass is low and the contact area is large.

Because the fuel mass in the tank changes over time, the factor τ is in fact not a constant. However, a fuel tank containing a fixed amount of 20,000 kg of fuel would have an estimated $\tau \simeq 10^5$ s, or about 2.8 h. Toward the end of the flight, there is relatively little fuel left in the tanks, and the OAT increases rapidly as the aircraft descends. Because the time constant is now greatly decreased, the fuel responds more rapidly to a change of outside temperature.

The system of differential equations is solved in the time domain by using a fourth-order Runge–Kutta method with the time step set by the flight trajectory data, i.e., the system Eq. (40) is fully synchronized with the flight mechanics. Setting the initial conditions is not straightforward: these temperatures are unknown, because warm or cold fuel can be loaded into the tanks. Fuel pumping in- and out of the tank clearly complicates the matter. Finally, a small difference in temperature between liquid and vapor phases has an effect on the numerical solution.

B. Tire Heating

Modelling the heating of a tire under a variable load is an exceedingly difficult problem. A pertinent analysis has been published by McAllen et al. [22,23], who demonstrated that both deformation characteristics and structural stresses do not undergo sinusoidal variation during a full revolution. These authors simulated the stress and strains with an equivalent two-dimensional finite element model and implicitly showed that the inelastic energy associated to the hysteresis of a cycle depends on the position of the element on a tire. For example, considerable differences can be found between the tire shoulder, the side wall, and the crown region.

In this context, we propose a simplified analysis that uses a limited set of data, such as those that can be found for a conventional transport aircraft. The tire temperature $\mathcal{T}_t$ is defined by the following operator:

$$\mathcal{T}(t) = f(t, F, \texttt{TireGeom}, \omega) \tag{20}$$

where F is the normal load, `TireGeom` is an operator that provides all the geometrical details (with and without deformation), ω is the rotational speed. Additional data that are required include at least the tire pressure, the type of gas and the mass of the tire. All the tires from one bogie are treated with the same normal load and thermal characteristics, although it is possible to include provisions for differential loading.

Some practical formulas for tire deflections are available in ESDU 86005 [24]. The tire dimensions are given according to some international standards. We assume that the width of the contact is equal to the width of the tire w. This assumption is a valid 1 in.the context of the overall approximations that are required to estimate the heat loads. The maximum length of the contact is l_c. This is conveniently found in terms of the relative vertical deflection δ_t/d_w, i.e., the ratio between the tire deflection and its nominal diameter [24]. From the vertical compression δ_t/d_w, we can calculate the compression volume dV. The tire deflection is conventionally given by $\delta_t\% = 100\delta_t/(d_w/2)$. The tire mass is calculated from the volume equation and a weighted specific mass. The rotational speed of the tire when the aircraft has ground speed U is $\omega = 2U/d_w$. The frequency of the loading is $f = \omega/2\pi$.

The increase in tire pressure due to loading F on the wheel is calculated iteratively. ESDU [24] suggest using the formula

$$\Delta p_t = 1.5p\left(\frac{w}{d_w}\right)\left(\frac{\delta_t}{d_w}\right)^2 \tag{21}$$

In our numerical method, this formula is inserted into a loop that allows the calculation of compression volume, contact length, pressure, and temperature rise in static conditions. Before entering this loop it is necessary to calculate the mass of the inflating gas. This calculation is done under unloaded conditions, by using the equation of the ideal gas. The next problem is to calculate the heat loads on both tire and inflating gas. A system of ODE similar to Eq. (15) is constructed. In this case, the vector of unknowns is

$$\boldsymbol{Y} = \{[Q, p, \mathcal{T}, \rho]_{\text{tire}}, [Q, p, \mathcal{T}, \rho]_{\text{gas}}\} \tag{22}$$

In practice, we solve for the heat balance, the pressure and the average temperature of both inflating gas and tire (six ordinary differential equation [ODE]). The system of Eq. (22) is synchronized with the takeoff equations, which is described by a similar set of eight ODE. Thus, the complete takeoff run (see further discussion in Sec. VI.B) with the tire heating theory requires the solution of 15 ODEs. If we further include the tire dynamics in the special case of one engine inoperative (OEI) operation and balanced field length calculation, the whole set of equations is coupled with the tire model described in Sec. VI.A.

The thermostructural model used in this analysis is shown in Fig. 6. An essential factor in the determination of the ODEs formally described by Eq. (22) is the normal load on the tire and the heat transfer rates. Starting from the normal loads, they depend on the position of the c.g., and hence on the takeoff trim. This is another requirement on multidisciplinary analysis. Once the aircraft has been trimmed for takeoff at the specified brake-release gross weight (BRGW), the loads on each tire are determined by static balance conditions solved at each time step.

The loaded tire deforms with a frequency f. Part of the energy is lost due to hysteresis. The hysteresis $\mathcal{H}$ is defined as the ratio between the energy lost and the deformation energy. The hysteresis depends at least from tire temperature and frequency. Following some research published by Lin and Hwang [25], it is reasonable to assume that $\mathcal{H}$ varies between 0.1 and 0.3. The highest values correspond to the lowest temperatures. Furthermore, the frequency effect seems to appear only at these temperatures. A secondary effect, albeit an important 1 at.high rolling speeds, is due to the centrifugal forces. One consequence of the centrifugal loads is the generation of a standing wave that causes a distortion on the side of the tire leaving the contact with the roadway. This condition is attributed to underinflation and should not normally be encountered during a takeoff operation.

The deformation work done on the tire during a full rotation is calculated from

$$\mathcal{W}_1 = F\Delta z\left(\left(\frac{\pi d_w}{l_c}\right) = F\left(\frac{dV}{\pi l_c w}\right)\left(\frac{\pi d_w}{l_c}\right)\right. \tag{23}$$

The factor Δz denotes the instantaneous *average* vertical deformation under load F, which causes a change in gas volume dV over an elliptical contact area $\pi l_c w$. The factor $\pi d_w/l_c$ is the correction from the instantaneous deformation to the total deformation during a full round. The work done during a time step dt is taken from

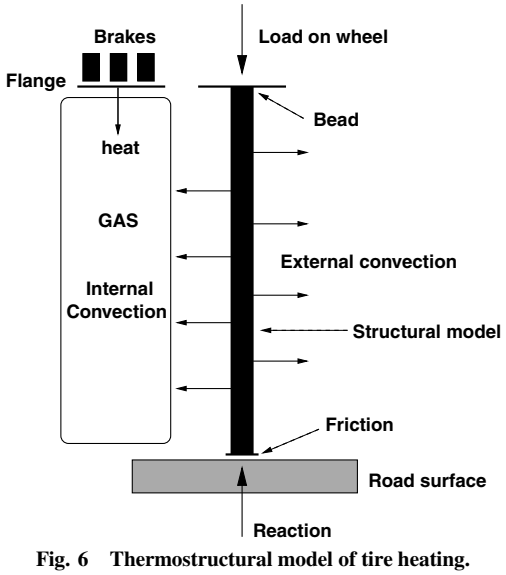

Fig. 6 Thermostructural model of tire heating.

$$\mathrm{d}\mathcal{W} = \mathcal{W}_1\left(\frac{\omega \mathrm{d}t}{2\pi}\right) \tag{24}$$

The work actually lost in the deformation is $\mathrm{d}\mathcal{W}\mathcal{H}$. This work is partly dissipated by the tire through external convection (E_c), through internal convection (E_g), through friction with the inflating gas (E_f), and by physical contact with the roadway (E_r). The remaining part (E_t) will serve to increase the thermal energy of the tire itself. Additional terms that may have to be included arise from the internal heat that is generated during the deformation and eventually by specific cooling systems. The radiation heat transfer to the gas is about 3 orders of magnitude lower than the other contributions and is not considered in the analysis.

Combination of Eqs. (23) and (24) and an appropriate value of the hysteresis are the key to the whole method. Finally, we need to find a way to estimate the heat loads, as expressed by

$$\mathrm{d}\mathcal{W} = \sum_i \mathrm{d}E_i \tag{25}$$

The forced convective heat transfer from the tire to the air can be calculated by using a suitable expression of the Nusselt number as a function of the Reynolds number. This relationship can be written as

$$Nu = aRe^b \tag{26}$$

The coefficients a, b depend on the problem; the Reynolds number is calculated from the aircraft speed and the rotational speed. For a thin rotating cylinder ($w/d_w \simeq 0.17$), the equation is

$$Nu = 5.88 \cdot 10^{-3} Re^{0.925} \tag{27}$$

There is the problem of justifying this correlation to the typical widths of an aircraft tire ($w/d_w \simeq 0.25$) and the surface roughness of a typical tire, which we have not fully investigated. The convective heat fluxes are

$$\dot{Q}_c = \frac{\mathrm{d}E}{\mathrm{d}t} = h_c A_c (\mathcal{T}_t - \mathcal{T}) \tag{28}$$

where $\mathcal{T}$ is the temperature of the gas (inflating gas or air) and

$$h_c = \left(\frac{k_c}{d_w}\right) Nu \tag{29}$$

The conductivity k_c is a function of the temperature, and is calculated from semiempirical relationships. The convective area A_c is calculated from the tire dimensions. The heat transfer to the inflating gas can be written with a similar expression, except that the Nusselt number and the heat transfer coefficient k_c are different and depend on the type of inflating gas. A suitable correlation is found from the data published by Seghir–Ouali et al. [26]. These data are relative to heated rotating cylinders, with an axial gas flow. The problem is governed by the rotating Reynolds number $Re_r = \omega d/2\nu$ and the axial flow Reynolds number Re_a. The data indicate that for $Re_r > 2.77 \cdot 10^5$, the Nusselt number is insensitive to the axial flow, which shows that the heat transfer is dominated by the rotation. At lower Re_r the axial flow has a role that increases as the rotation decreases. Data are available for $Re_a = 0$, which corresponds broadly to the present case, although there would be the problem of accounting for the end-wall effects.

The heat transfer with the roadway occurs through the contact surface A_c that has an elliptic shape, with axes l_c and w; the resulting formula is

$$\dot{Q}_r = \frac{\mathrm{d}E_r}{\mathrm{d}t} = k_{c_t} A_c (\mathcal{T}_t - \mathcal{T}_{\text{road}}) \tag{30}$$

where k_{c_t} is the thermal conductivity of the tire. Finally, the energy accumulated by the tire itself is described by

$$\dot{Q}_t = \frac{\mathrm{d}E_t}{\mathrm{d}t} = C_{p_t} m_t (\mathcal{T}_t - \mathcal{T}) \tag{31}$$

Equation (31) does not differentiate between parts of the tire, and will only provide an average tire temperature. Local difference in temperatures have been measured by McCarty and Tanner [27], who concluded that the temperature along the inner walls are lower than the temperatures around the outer surface. This result also implies that the road contact is a more important factor.

The heat coefficient can be estimated by weighted average of its components. These are: rubber (about 80%); steel chords (5%) ; textile fabrics (15%), although some manufacturers quote different proportions. The exact composition of a tire is proprietary information. Average heat transfer coefficients are: rubber: $C_p =$ 1.5 kJ/kg K; steel: $C_p = 0.46$ kJ/kg K; nylon-based fabrics: $C_p = 1.7$ kJ/kg K. The weighted average is 1.478 kJ/kg K. There can be considerable differences with real tires. Furthermore, there can be special mechanisms that minimize tire heating by means of cooling.

The change in energy for the gas derives from the convective term specified by Eq. (28) and by the friction between the inner tire and the gas. The movement of the inflating gas inside the tire during rotation is not amenable to simple modelling. Thus, for the purpose of the present analysis some educated approximations are required to establish a suitable value of friction between the gas and the internal walls of the tire.

VI. Flight Mechanics Model

The deployment and retraction of the undercarriage units and the flight control surfaces is impulsive. This is a result of the relatively large time step that is used for most flight mechanics calculations. Thus, there is an impulsive change in aerodynamic characteristics and noise response (the latter item is discussed separately).

At the basic level one is interested in estimating state–state cruise performance, which is where most fuel is burned. In fact, a considerable amount of work has been devoted to the optimization of cruise procedure, and the methods for this analysis are now well established. However, at a fundamental level (such as preliminary design), cruise analysis still relies on the use of a very simple range equation that gives a closed-form solution.

Expanding from these requirements, it is possible to model several thermodynamic aspects of the airplane, including icing, fuel temperatures (an item of interest during long-haul flights), tire performance at rejected takeoff and large takeoff and landing weights, cabin environment (ambient temperature and pressure, air conditioning), and its requirement on the APU.

A. Ground Performance

The tires' thermostructural model relies on the normal load. If F_m and F_n denote the normal load of the total main and nose undercarriage, respectively, then the normal load per tire is calculated by dividing these quantities by the number of wheels in each undercarriage unit: is $F_{m1} = F_m/n_m$, $F_{n1} = F_n/n_n$.

The normal loads are calculated by using the pitching moment equation of the airplane with respect to the c.g.. With reference to Fig. 7, the total rigid-body moment around the c.g. is

$$M_y = M_{ow} + \underbrace{(L_t x_t + L_w x_w)}_{\text{lift}} + \underbrace{(F_m x_m + F_n x_n)}_{\text{reaction}} + \underbrace{(\mu_{rm} F_m z_m + \mu_{rn} F_n z_n)}_{\text{friction}} + T z_t \tag{32}$$

where M_{ow} is the wing's pitching moment, the underscores t and w denote horizontal tail plane and wing, respectively[†]; the remaining quantities are indicated in Fig. 7. Equation (32) does not contain the drag term. Its application point is not clearly determined, so we assume that it lies on the line of the longitudinal axis through the c.g.. Three cases are possible: 1) all undercarriage on the ground, which implies $M_y = 0$; 2) nose undercarriage liftoff (airplane rotation), in

[†]This analysis assumes that the aerodynamic coefficients are calculated by normalizing with the own wing area, $C_{L_t} = L_t/qA_t$, etc.

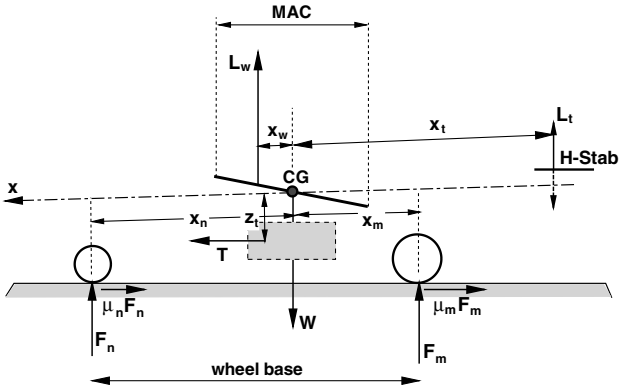

Fig. 7 Aircraft forces on the ground.

which case $F_n = 0$ and the airplane has a rotational acceleration; and 4) liftoff, causing $F_m = F_n = 0$; at liftoff Eq. (32) is no longer used. In the first instance, the solution of the equation provides the instantaneous normal loads. With reference to Fig. 7, the vertical equilibrium of a rigid body is

$$F_m + F_n = L_w + L_t - W \tag{33}$$

Rearranging Eq. (32) with $M_y = 0$, the solution system can be cast in matrix form as follows:

$$\begin{bmatrix} 1 & 1 \\ (x_m + \mu_{rm} z_m) & (x_n + \mu_{rn} z_n) \end{bmatrix} = \begin{bmatrix} F_m \\ F_n \end{bmatrix} = \begin{bmatrix} L_w + L_t - W \\ -(L_t x_t + L_w x_w) - (T z_t + M_{ow}) \end{bmatrix} \tag{34}$$

The knowledge of the position of the c.g., the aerodynamic center and the lift contributions from wing and horizontal stabilizer are required. For some load conditions there is no solution.

Combination of some mathematical models presented earlier can be used for complex simulations, such as the complete tire dynamics during a rejected takeoff. Some key aspects of interest in-flight simulation and airplane certification include the determination of the minimum control speed on the ground V_{MCG} and the tire load, in the form of heating and overall dynamics. The former problem requires the combination between the aerodynamics of the vertical tail, the controls of the airplane, the tire dynamic performance and the ground characteristics.

With reference to the twin-engine airplane shown in Fig. 2, the yaw moment balance around the center of the main landing gear) is

$$M_{\mathrm{vt}} = T b_t - Y_n w_b \tag{35}$$

where M_{vt} is the yaw moment created by the vertical tail unit as a consequence of a rudder deflection ξ; b_t is the moment arm of the thrust asymmetry, w_b is the wheel base, and Y_n is the side force on the nose wheels in absence of lateral skidding. The side force is equivalent to the cornering force if the plane of rotation is aligned with the ground velocity. All forces and moments are a function of the ground speed. Consider the rudder in its maximum design deflection $\xi_{\max}$. If the corresponding tail moment $M_{\mathrm{vt}} > T b_t - Y_n w_b$, then lateral control can be achieved with the rudder; if the tail moment is $M_{\mathrm{vt}} < T b_t - Y_n w_b$, then the rudder deflection can be decreased and lateral control can be achieved by nose wheel steering. The minimum control speed has to be lower than the liftoff speed.

Federal Aviation Regulations (FAR) section 25.149 defines the limits for the determination of V_{MCG} on the ground. In particular, the regulations require that the aircraft with OEI has a path on the runway that does not deviate laterally by more than 30 ft (9.15 m) at any point. This speed must be determined with the airplane at the most critical condition, the most unfavorable position of the c.g. and takeoff weight. The moment generated by the vertical tail is

$$M_{\mathrm{vt}} = L_{\mathrm{vt}} x_{\mathrm{vt}} = \frac{1}{2} \rho U^2 A_{\mathrm{vt}} C_{L_\xi} \xi x_{\mathrm{vt}} \tag{36}$$

where A_{vt} is the vertical tail's area and x_{vt} is the distance between the line of action of the rudder lift and the center C of the main landing gear, C_{L_ξ} is the lift-curve slope of the tail-rudder combination.

Assuming $\xi = \xi_{\max}$, and solving for the ground speed $U = V_{\mathrm{MCG}}$, the yaw equation becomes

$$V_{\mathrm{MCG}}^2 = \frac{2(T b_t - Y_n w_b)}{\rho A_{\mathrm{vt}} C_{L_\xi} \xi_{\max}} \tag{37}$$

The solution of Eq. (37) depends on the limit side force on the nose tires. A semiempirical method for calculation of this force is given by ESDU [28], although it requires the yaw angle of the tire. We consider the case of an unbraked wheel. For a given value of the normal load on the tire F_n, we are interested in finding the limit side force (cornering force) on the tire Y_n before the tire starts skidding sideways. In practice, before such condition occurs, the tire will operate in yaw. The tire's yaw introduces a major complication. To begin with, as the aircraft accelerates, it gains lift and unloads the nose gear. As the nose gear is unloaded, its cornering force decreases. Thus, unless dynamic lift grows quickly, the velocity V_{MCG} will be inconveniently high. In fact, it is possible that there is a range of ground speeds at which it is not possible to control the aircraft, either by nose gear steering or by vertical tail and rudder. In a second instance, it is necessary to decide whether the nose tires are operating in yaw, because the cornering force depends on this angle. Assume that tire's yaw angle is sufficiently small. The ratio between these two forces is the lateral friction coefficient

$$\mu_{rs} = \frac{Y_n}{F_n} \tag{38}$$

From the analysis of data published by Dreher and Tanner [29] on a number of tires under dry, wet and flooded runways, the sideways friction coefficient is a parabolic function of the yaw angle.

The solution is iterative, with the true air speed (TAS) adjusted so that the condition $M_{\mathrm{vt}} - (T b_t - Y_n w_b) = 0$ is satisfied within a small tolerance. An example of V_{MCG} calculation is shown in Fig. 8 for the conditions specified in the caption. The result indicates that $V_{\mathrm{MCG}} < V_{\mathrm{LO}}$, as expected. The calculation assumed that the maximum rudder deflection is 10 deg and that the aircraft drifts laterally by 30 ft (9.15 m) over the distance of 1000 m.

The result is clearly dependent on several factors, including conditions of the runway, tire tread (ribbed or smooth), wind speeds and direction (headwind or tailwind), position of the c.g., tire yaw angle, maximum rudder deflection, roll effects, all cases that can be evaluated separately or in combination.

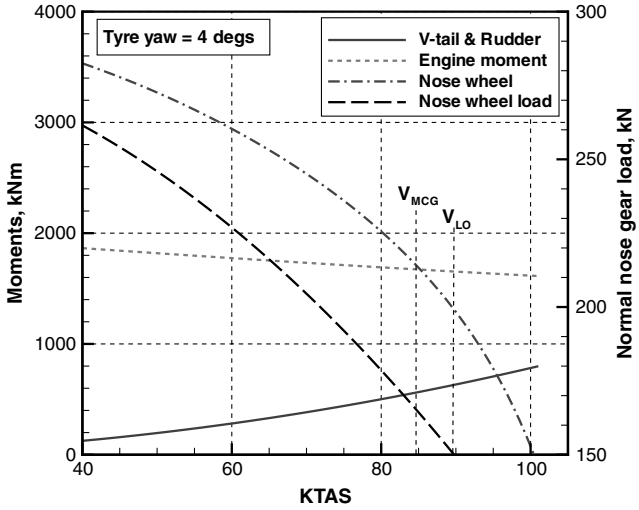

Fig. 8 Calculated V_{MCG} for Airbus A300-600 model; BRGW= 145.0 ton; standard day, no wind, dry runway.

B. Takeoff Model

There are several models for airplane takeoff available in the technical literature, that provides models with various levels simplifications. It is not possible to review the subject in this context, but it will suffice to mention ESDU [30,31] for rigorous methods in deriving the equations. The takeoff is described by a system of ODE in the time domain formally described by

$$\frac{\mathrm{d}\boldsymbol{Y}}{\mathrm{d}t} = \mathcal{F}(t) \tag{39}$$

The differential takeoff equations are

$$\dot{\boldsymbol{Y}} = \{\dot{u}, \dot{x}, \dot{v}, \dot{z}, \dot{\alpha}, \ddot{\alpha}, \dot{z}_n, \dot{m}_f\} \tag{40}$$

These equations describe the horizontal acceleration $\dot{u}$ and ground speed $\dot{x}$; vertical acceleration $\dot{v}$ and climb rate $v_c = \dot{z}$, rotational acceleration $\ddot{\alpha} = \dot{\omega}_y$ and rotational velocity ω_y, vertical displacement of the nose shock absorber $\dot{z}_n$ from the ground, fuel flow $\dot{m}_f$. All other quantities are calculated outside the differential system. Additionally, there are two algebraic equations for the rolling resistance and the net thrust (from the static analysis of the engine model). The rolling coefficients μ_m and μ_n are calculated following [32] for a variety of roadway conditions and normal loads F_m and F_n [Eq. (34)]). The system of Eqs. (22) and (40) is solved in the time domain using a fourth-order Runge–Kutta integration.

All the aerodynamic coefficients are called in real time through a functional such as Eq. (7). The system of Eq. (39), along with the ancillary equations, is coupled with the tire thermophysics (Sec. V.B and rolling dynamics (Sec. VI.A), for calculations such as normal and rejected takeoff, and balanced field length. A number of switches are introduced to take into account a series of rapid events:

$$\texttt{TakeOffSwitch} = \{\texttt{Brake}, \texttt{TireLiftOff}, \texttt{ShutDown}, \texttt{Flap}, \cdots\} \tag{41}$$

In keeping with regulations and standards (for example, FAR section 25.109), time-lag operators are built into Eq. (41). All the switches are instantaneous, except the engine thrust, which decays exponentially.

The integration of the ODE is done from brake-release point ($t = 0$), where all the dependent parameters are known, and are solved iteratively to get the flap setting right. Flap steps of 5 deg are used by default. The optimal condition satisfies a minimum climb rate over the conventional FAR screen, subject to all the specified external factors, including atmosphere [Eq. (3)] and airplane state [Eq. (2)]. If the initial climb rate is below a threshold, the flap is increased, and the integration is restarted. Normal integration time-steps are 10^{-2} s.

C. Climb and Descent Models

The correct mathematical formulation of an optimal climb problem is a two-value boundary problem, with initial conditions assigned and part of the final initial conditions also assigned. There is no way a pilot will be able to find an optimal control procedure of the airplane that satisfies any of these requirements. The solution is assigned to the flight computer, that does in principle what we set out to do next.

The climb problem is defined by a set of five primary differential equations for the aircraft position $\dot{\boldsymbol{x}}$, climb rate $\dot{v}_c$, climb angle $\dot{\gamma}$, and fuel flow $\dot{m}_f$. A transformation from the time domain to the space domain is sometimes required. If $\boldsymbol{Y}$ denotes the vector of the left-hand side variables, this is done through

$$\frac{\mathrm{d}\boldsymbol{Y}}{\mathrm{d}h} = v_c\left(\frac{\mathrm{d}\boldsymbol{Y}}{\mathrm{d}t}\right) \tag{42}$$

The engine performance is calculated with a predictor-corrector scheme. First, the engine deck is required to perform an engine state calculation for a given (h, M); this produces a vector of variables at the limit of the envelope, $\mathcal{E}_{\text{limit}}$. The second step requires to use a fraction of the limit net thrust, via a throttle Π. The new value of F_N is then used to calculate the engine state $\mathcal{E}$ in the usual inverse mode.

The climb to initial cruise altitude (ICA) of a transport aircraft is generally done in three or four phases, as illustrated in Fig. 9 and described below:

1) Constant calibrated air speed in knots (KCAS) or indicated air speed in knots (KIAS) up to flight level FL-100 (10,000 feet; 3,048 m).

2) Acceleration at constant altitude (FL-100) to a chosen true air speed.

3) Constant KCAS (or KIAS) up to a crossover altitude (discussed below).

4) Constant Mach number to the ICA.

For some flight conditions it is possible that the final phase is missing. However, when this phase is required, the TAS and the calibrated air speed (CAS) decrease as the aircraft climbs to the tropopause. Furthermore, the takeoff KCAS is generally well below the prescribed KCAS1. Therefore, the aircraft will have to accelerate from the initial takeoff speed to KCAS.

The climb performance is done with a reduced set of free parameters. These are the first-segment CAS, the final TAS of the second segment, the third-segment CAS, the cruise Mach number and the ICA; KTAS1 is uniquely determined by KCAS1 and KCAS2 is determined by the flight level and KTAS2. Thus, we need to specify only KCAS1, KTAS2, the cruise Mach and the ICA. On the other hand, both cruise Mach number and optimal ICA can be optimised by the flight management computer ahead of the climb, so that the optimal climb is a two-boundary value problem with known conditions at the terminal point.

The descent procedure follows a similar constrained path from the top of descent (or final cruise altitude) down to 1500 ft, after which the aircraft is guided to the airfield on the basis of more stringent control procedures. First, the aircraft is allowed to descend at constant Mach to an altitude where it reaches a target CAS. In the second stage, it maintains constant CAS to 10,000 ft (FL-100, 3048 m). In the third stage it decelerates at a constant altitude to reach a target CAS (below the previous one). The final stage is a descent at a constant CAS to 1500 ft.

D. Cruise Model

The critical parameter required by a cruise analysis is the specific air range (SAR), which is a point-performance parameter defined by

$$\mathrm{SAR} = \frac{\mathrm{TAS}}{\dot{m}_f} \tag{43}$$

A full integration between the propulsive and aerodynamic terms is required to solve Eq. (43) for a given all-up weight (AUW) and atmospheric conditions. This is inferred from the fuel flow, which

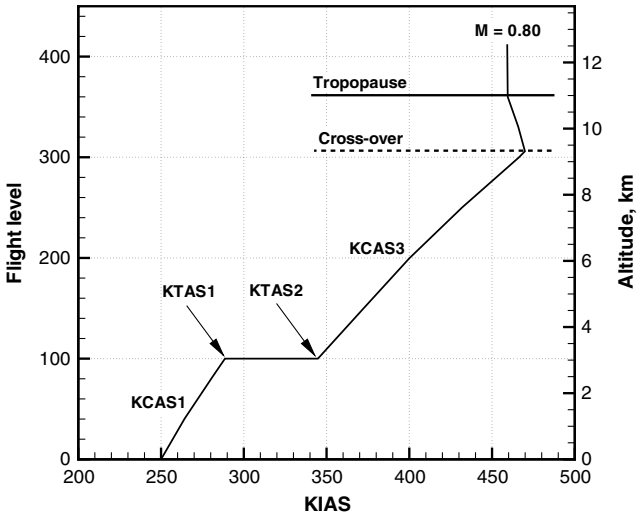

Fig. 9 Typical climb schedule of transport aircraft.

depends on the thrust level (an input signal), and hence on the aerodynamic drag.

The analysis of the optima in the SAR equation is used to determine iteratively the initial cruise conditions. The optimization itself consists of a search with a steepest descent method along two directions: Mach number and cruise altitude. The initial cruise altitude is then adjusted to the nearest conventional flight level (FL):

$$(\mathrm{FL}, M)_{\mathrm{cruise}} \rightarrow \max[\mathrm{SAR}(h, M)] \tag{44}$$

The final stage in the cruise optimization contains a fairly large number of parameters. If n is the number of constant-altitude steps, the number of climb steps is $n-1$. The final segment is always a cruise. The number of climb steps is

$$n - 1 = \frac{\Delta h}{\mathrm{FLS}} \tag{45}$$

where FLS is the flight level separation. For example, if the adjusted climb is $\Delta h = 4000$ feet (1219 m) and FLS = 100 (or 1000 feet), then $n = 5$ (four climbs; five cruise segments). The distances flown in the cruise mode are called x_i and the distances covered by the climb steps are called x_{c_i}. The constraints are

$$X = \sum_{i}^{n} x_i + \sum_{i}^{n-1} x_{c_i} \tag{46}$$

$$\Delta h = (n-1)\,\mathrm{d}h \tag{47}$$

The total number of free parameters is $2n-1$, i.e., n constant-altitude stage lengths and $n-1$ climb rates between flight levels. Mathematically, such a problem is quite complex. Practical solutions deal with specified climb rates and cruise stages of equal magnitude, except the last one. Thus, the number of free parameters is reduced to 3 (two cruise stage lengths and one climb rate). An alternative cruise procedure relies on the change of flight level based on the AUW of the aircraft. There are two cruise options implemented: possibilities:

1) *Low Profile*: The step climb starts at the weight corresponding to the intersection between the next flight level and the theoretical optimal altitude. The flight profile is always below the optimal cruise altitude; the aircraft has a better manoeuver margin. This procedure requires a limited number of intermediate calculations to estimate the AUW at the switch point.

2) *Middle Profile*: The step climb starts when the SAR at the higher flight level is better than the SAR at the current flight level. This procedure requires the calculation of the SAR at two flight levels at each time step. It is computationally more demanding, and for this reason it is presently not used.

Finally, a sensitivity analysis on Eq. (44) can be carried out to study cruise altitude flexibility, and thus alternative cruise options, such as contrail avoidance.

E. Mission Optimization

This is a case of multidisciplinary integration at the top level of our flowchart, Fig. 1. Aircraft mission optimization deals with the fuel planning and the determination of optimal trajectories that provide the most economical operation of the airplane. In this section we deal with the former problem. The determination of optimal Mach numbers, cruise altitudes, climb strategies, etc., are part of a larger context, partially discussed earlier. For a given mission requirement (range and payload), the fuel and the gross takeoff weight are determined iteratively through the operator

$$\texttt{MissionFuel} = f(m_f^*, m_{\mathrm{pay}}, X_{\mathrm{req}}, \texttt{Atmosphere}, \cdots) \tag{48}$$

The independent parameter m_f^* is an estimated value of the total fuel; m_{pay} is a specified payload (including services of all types) and X_{req} is the required range. For a given m_f, Eq. (48) is called by a driver operator, and determines the optimal trajectory and the corresponding fuel. This includes items such as rollout fuel, the takeoff fuel and the reserve fuel according to the prevailing regulations. Then the driver calls Eq. (48) with the new value of the fuel, and repeats the process. To achieve convergence, an under-relaxation parameter must be used. If W_n denotes the ramp weight at iteration n, its value at the new iteration count $n+1$ is calculated from

$$W_{n+1} = \frac{1}{2}(W_n + W_{n-1}) \tag{49}$$

Without under-relaxation, it is possible that the fuel planning procedure diverges, as the ramp weight would increase at each successive iteration. Convergence is achieved in a few iterations if the initial guess is sufficiently close to the correct result. If the airplane is known, and the range required is comparable to the design range, a good initial guess is

$$m_f^* = \left(\frac{X_{\mathrm{req}}}{X_{\mathrm{design}}}\right)\texttt{FuelCapacity} \tag{50}$$

On convergence, the trajectory and segments thereof are stored in a database, along with the other airplane parameters, for use in later analysis, such as the aircraft noise, discussed in Sec. VII. The complete analysis of the mission returns a detailed operational weight breakdown, including OEW, payload, fuel (total, mission segments, reserve, unusable), operational items, crew weight contribution.

The mission cannot be fulfilled if: 1) the payload is greater than the maximum design payload, 2) the range is greater than the ferry range, and 3) the ramp weight exceeds the design maximum ramp weight, and in any other case in which a segment weight (BRGW, maximum takeoff weight, and maximum landing weight) exceeds the certified airplane parameters. Numerically, there is a possibility of a weight divergence if the airplane is forced to operate at the limit or beyond of the envelope (large payload and long range).

The inverse problem, i.e., the calculation of the aircraft range corresponding to a fixed fuel and payload is a more elaborate process, because of the implicit relationship between trajectories, auxiliary power system (APU) services and ramp weight. It is common practice to use the Breguet range equation for the inverse problem, although strictly speaking it only applies to the cruise range and not the mission range. The Breguet equation carries a number of simplifications that are powerful for a preliminary design approach, but not for a detailed analysis such as the one that is proposed in this study.

In fact, the problem is solved iteratively. A first value of the range is calculated with a procedure `MissionRange`, that requires a first guess of the cruise Mach number and the ICA. Then there are the following steps: 1) calculate the fuel from ramp up to the ICA by using the same method as `MissionFuel` (this includes taxi out, takeoff, climb to ICA, and APU fuel to that point); 2) calculate the extended all out fuel $m_{f_{\mathrm{ext}}}$, with a method described by Torenbeek [33], to take into account holding and diversion procedures, and 3) using the procedure indicated in Sec. VI.C, calculate the descent fuel m_{f_d} and distance x_d from the ICA (the final cruise altitude is indeterminate), with an initial weight

$$W = \mathrm{GTOW} - (m_{f_{\mathrm{ext}}} - m_{f_{\mathrm{res}}})g \tag{51}$$

and finally, 4) calculate the cruise range with

$$X_{\mathrm{cruise}} = \frac{\mathrm{TAS}}{\mathrm{TSFC}}\left(\frac{L}{D}\right)\log\left(1 + \frac{m_{f_{\mathrm{cruise}}}}{m_f - m_{f_c}}\right) \tag{52}$$

where the cruise fuel is

$$m_{f_{\mathrm{cruise}}} = m_{f_{\mathrm{usable}}} - (m_{f_c} + m_{f_d} + m_{f_{\mathrm{ext}}}) \tag{53}$$

The propulsive and the aerodynamic terms are calculated from the condition of steady-state flight. The first estimate of the aircraft range is

$$X_1 = x_c + x_d + X_{\mathrm{cruise}} \tag{54}$$

It is not possible to establish a priori whether Eq. (54) is an over or underestimate. However, its value is further improved with an iterative algorithm based on the bisection method [34]. More

specifically, the inverse procedure `MissionRange` is called once; the direct procedure [Eq. (48)] is called as many times as required to converge within a tolerance. Assuming that the error is Δx around X_1, n bisection steps should converge to $\Delta x/2^n$. Note that `MissionFuel` itself is iterative; if m are the steps required to convergence, the inverse problem will converge in $n \times m$ steps; `MissionFuel` always returns optimal Mach numbers and trajectories. The complete numerical method is used for calculating selected operation points in the payload-range chart (maximum-payload range; maximum-fuel range; ferry range).

VII. Aircraft Noise Model

The calculation of aircraft noise relies on the state of the airplane over a trajectory [Eq. (2)] and on the atmospheric conditions [Eq. (3)]. There are two ways of including a noise model. First, the acoustic equations can be synchronized with the flight mechanics, so as to provide the acoustic sources as part of the overall solution. However, because the optimal trajectories are calculated iteratively, such a method would require the acoustic model to run as many times as required for the trajectory to converge. Another limitation of this approach is that for the acoustic model to be reliable the time step of the flight mechanics equations would have to be decreased considerably, which would further slow down the process. The strategy that we follow is to decouple the two sets of models, maintain the time steps that are required by the flight mechanics, and eventually determine a more refined trajectory with a smaller time step by high-order interpolation. This logical decoupling also results into two nearly independent modules (or software packs); the latter one is called `FLIGHT-noise`. The communication between flight mechanics and aircraft noise is limited to the following vector

$$\texttt{NoiseComm}(t) = \{W, \boldsymbol{X}, \boldsymbol{V}, T, \texttt{Atmosphere}, \texttt{Controls}\} \tag{55}$$

where $\boldsymbol{X}_{(t)}$ is the vector position of the aircraft's c.g. with respect to a reference on the ground $\boldsymbol{x}_o$; $\boldsymbol{V}_{(t)}$ is the velocity vector; T is the net thrust. The latter parameter is used to calculate the engine in reverse mode as indicated earlier (see also Fig. 4), and it represents a considerable advantage, not least because all the aerothermodynamic parameters required by the models for propulsive noise can be calculated directly as a response to a single input signal (the net thrust). The vector `Controls` defines the sequence of control actions on the airplane and replaces Eq. (2). The actual distance between one noise source S and the receiver is $\boldsymbol{r} = \boldsymbol{X} + \boldsymbol{r}_s$, i.e., the vector sum between the c.g. position and the position of the source with respect to the c.g.. The noise itself is formalized by the following equation:

$$\texttt{Noise}(t) = \boldsymbol{f}(\texttt{State}, \texttt{EngineState}, \texttt{Atmosphere}, t) \tag{56}$$

The parameter `Noise` refers to a variety of quantities, including: 1) sound pressure level (SPL) for a given component or system, 2) SPL for the complete airplane (OSPL), and 3) OSPL weighted on the A-scale (OASPL). All these quantities depend on a single position of the airplane. Furthermore, integral metrics can be introduced, such as the effective perceived noise (EPN) and the sound exposure level, which depend on a complete trajectory. The determination of the EPN is in fact required in the noise certification process [35] of the airplane, while the noise point-performance is more useful at the analysis and design stage.

Storage of all the data produced by `FLIGHT-noise` leads to large matrices of acoustic contributions in terms of component, frequency, time and position on the ground. Thus, if OASPL is the relevant metrics for a particular analysis, then

$$\text{OASPL} = \boldsymbol{f}(\boldsymbol{r}, t, f) \tag{57}$$

Equation (56) contains a number of subtasks:

1) Determination of the active noise components via the vector `Controls` to determine the relevant switch to be communicated to `FLIGHT-noise`.

2) Determination of the noise influence of each active component (power spectral densities).

3) Determination of the interference noise among relevant sources.

4) Propagation and absorption of the noise source to a receiver on the ground, including Doppler effects.

The development of a suitable aircraft noise model relies on the well-established method of components pioneered by Fink [36] and Fink and Schlinke [37], but with the inclusion of some interference factors.

The propulsion noise model uses Heidmann's [38] fan and compressor noise theory (with modifications to account for multi-stage compressors), ESDU's method for gas turbine combustors [39] (with modifications to interpolate databases of experimental data over a range of polar emission angles), the four-source model of Fisher et al. [40,41] for the coaxial jet noise (modified to account for the effects of free flight). One important interference effect is the jet shielding, that intervenes whenever the airplane performs three-dimensional manoeuvres and when the receiver is not right below the aircraft. Some models exist to account for the shielding effect on a twin-engine configuration [42–44]. In principle, for a four-engine configuration there are six interference contributions, i.e., the jet shielding effects due the number of permutations, 4!, but this model has not been tested.

The airframe noise models include the landing gear noise prediction of Guo [45] and Guo et al. [46,47] (with corrections to the empirical factors), Lilley's lifting surface model [48], Brooks and Humphrey's flapside edge noise [49], along with some models from ESDU [50] for the determination of such aspects as the effects of high-lift systems from a limited amount of geometrical parameters (slats, spoilers, etc.).

Because of the independence of most of these underlying theories, each noise component can be treated as a separate entity from a simulation standpoint, and can be eventually replaced by improved and more comprehensive models. Once the sources of noise are determined, there remain some important steps before the noise is recorded at a receiver point. These operations are termed `SignalAnalysis`:

$$\texttt{SignalAnalysis} = \{f, \boldsymbol{r}, \texttt{Atmosphere}\} \tag{58}$$

There are several processes involved in the operator of Eq. (58), including Doppler corrections, atmospheric absorption and boundary effects. The first operation is straightforward, because it only depends on the frequency, the effective Mach number, and the polar emission angle. The atmospheric absorption uses the model defined by ISO 9613-1 [51], with an appropriate integration scheme to account for variable-density atmosphere. The boundary effects are considered by approximating the ground as an infinite surface with a given impedance. Our ground reflection model follows the method of Attenborough [52] and ESDU [53]. These theories require external parameters, such as atmospheric turbulence [Eq. (3)] and type of ground.

The geometrical model formally defined by Eq. (2) is now used to determine a fairly large number of parameters required by the noise model, in particular all the geometrical details required for the landing gear noise (as described by Guo [54]). Likewise, the geometrical details of the gas turbine engine are used for various propulsive noise calculations. Note that often there is a lack of coherent data. For example, in the case of undercarriage units not all the geometrical details are available. The case of the gas turbine engine is even more restrictive: data such as rotor-stator spacing, number of compressor blades, nozzle area are determined from statistical analysis from a few known engines.

VIII. Validation Strategies

A full validation of the model presented must follow several steps at four integration levels, as shown in Fig. 10. There is a validation

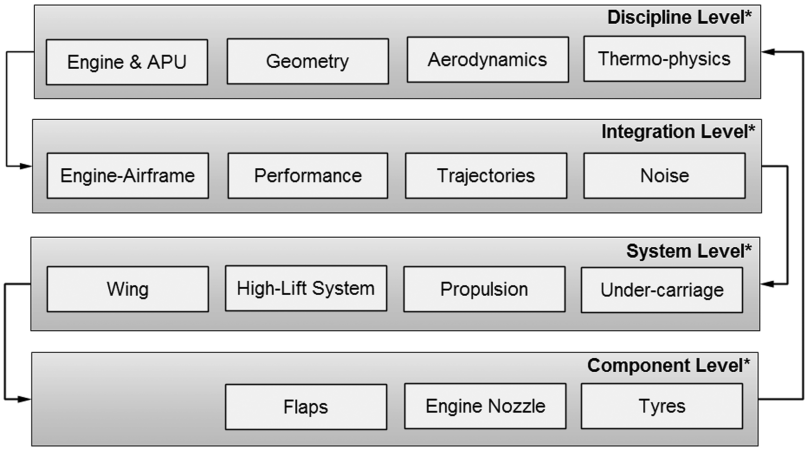

Fig. 10 Code validation strategy on multiple levels; [*] denotes selected disciplines.

procedure at a discipline and multidisciplinary level; then there is a validation at a component level (for example, engine nozzle) or system (undercarriage unit). Disciplines such as aerodynamics are evaluated as a whole (i.e., drag of the complete airplane), as components (for example, wing) and system (for example, landing gear). Because of the large number of possibilities that can be inferred from Fig. 10, we consider a limited, yet representative set of test cases.

The first aspect to consider is that there is not a coherent set of data for any airplane, and in some case the data available are incorrect. Therefore, we have to construct several models, isolate specific components, and program a special software pack for validation purposes. However, the use of different airplanes aids the debugging process, which is not a completely rational enterprise, and often overlooked. The models that have been used in the present analysis include the Boeing B-737-900(CFM56-5C4), Boeing B-777-300 (GE-90-92B), Boeing B-747-400(CF6-80C2A1), Airbus A-300-600(CF6-80C2A3) and Airbus A-380-861(GP-7270), although not all of them are shown. Additionally, there are isolated test cases, as discussed below.

A. Geometry Models

Starting from the geometrical modelling, in Fig. 11 we show a test case for the Airbus A-380-861 powered by GP-7270 gas turbine engines. The figure shows the distribution of cross-sectional area to demonstrate that all the major parts of the airplane match together. A summary of wetted areas is given in Table 2, which is copied from a computer printout. The total wetted area in cruise configuration is estimated at 4078.5 m^2 (or 43,900 ft^2), with a ratio wet-area/wing-area = 5.60. The estimated error with respect to the actual data is $\pm 1\%$. A sensitivity analysis option has been developed to understand the role of the wetted areas on the overall profile drag coefficient, and hence on the cruise performance of the airplane.

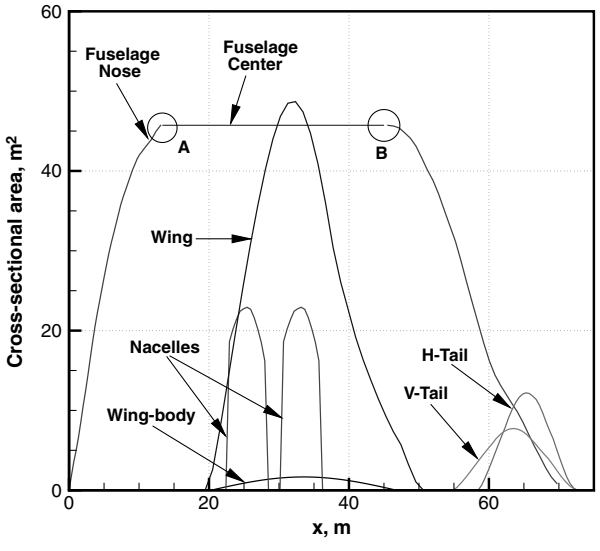

Fig. 11 Cross-sectional area distribution of the Airbus A380-861.

B. Propulsion System

Figure 12 shows a limited set of simulated engine parameters for the high bypass turbofan engine GP-7270. Graph 12a shows that the relationship between throttle and net thrust is nearly linear at all altitudes. The main parameter of the airframe-engine integration is the relationship between net thrust and fuel flow (graph 12b). This relationship is not linear, although the scales do not allow a full appreciation of this fact. The remaining graphs show parameters at the engine nozzle, which are used exclusively for nozzle/jet noise calculations. Validation of the engine performance model, which is key to the whole framework, is currently not done due to lack of suitable reference data.

C. Integration Strategies

Because the engine (for example, Fig. 12) cannot be directly validated with actual engine charts, a full engine-airframe integration (Level 2 in Fig. 10) it determined indirectly, by considering optimal points in the SAR charts, and changes in aircraft range corresponding to changes in payload.

With respect to the former point, a typical SAR chart is shown in Fig. 13 for the Boeing B-777-300-GE at a gross weight 254.5 tons. The long-range cruise Mach number (LRM) is estimated at 0.835 at flight levels between 310 and 330; increasing to FL-350, the LRM is slightly reduced to 0.834. These data compare relatively well to the claimed typical cruise Mach equal to 0.84, although it is not generally disclosed that the best cruise Mach is a variable parameter that depends on AUW and atmospheric conditions. An internal optimization procedure based on the data shown in Fig. 13 is used to determine the ICA and the cruise Mach at the initial cruise weight.

With respect to the second point, a verification is done through the derivative

$$\left(\frac{\mathrm{dZFW}}{\mathrm{d}x}\right)_{\mathrm{BRGW}}$$

where ZFW denotes the zero-fuel weight. At a constant BRGW, this derivative must be negative; its value is a sensitivity parameter that is proportional to the SAR [Eq. (43)]. Thus, it can be directly associated to the fuel flow. The advantage of this approach is that it is possible to find performance charts from the airplane's operating manual that allow such a comparison, although the conditions under which the charts are derived are never fully specified.

The next example of integration is the payload-range chart for the Airbus A380-861-GP7270. This chart is one of the most important performance indicators of any flight vehicle; yet, there are no

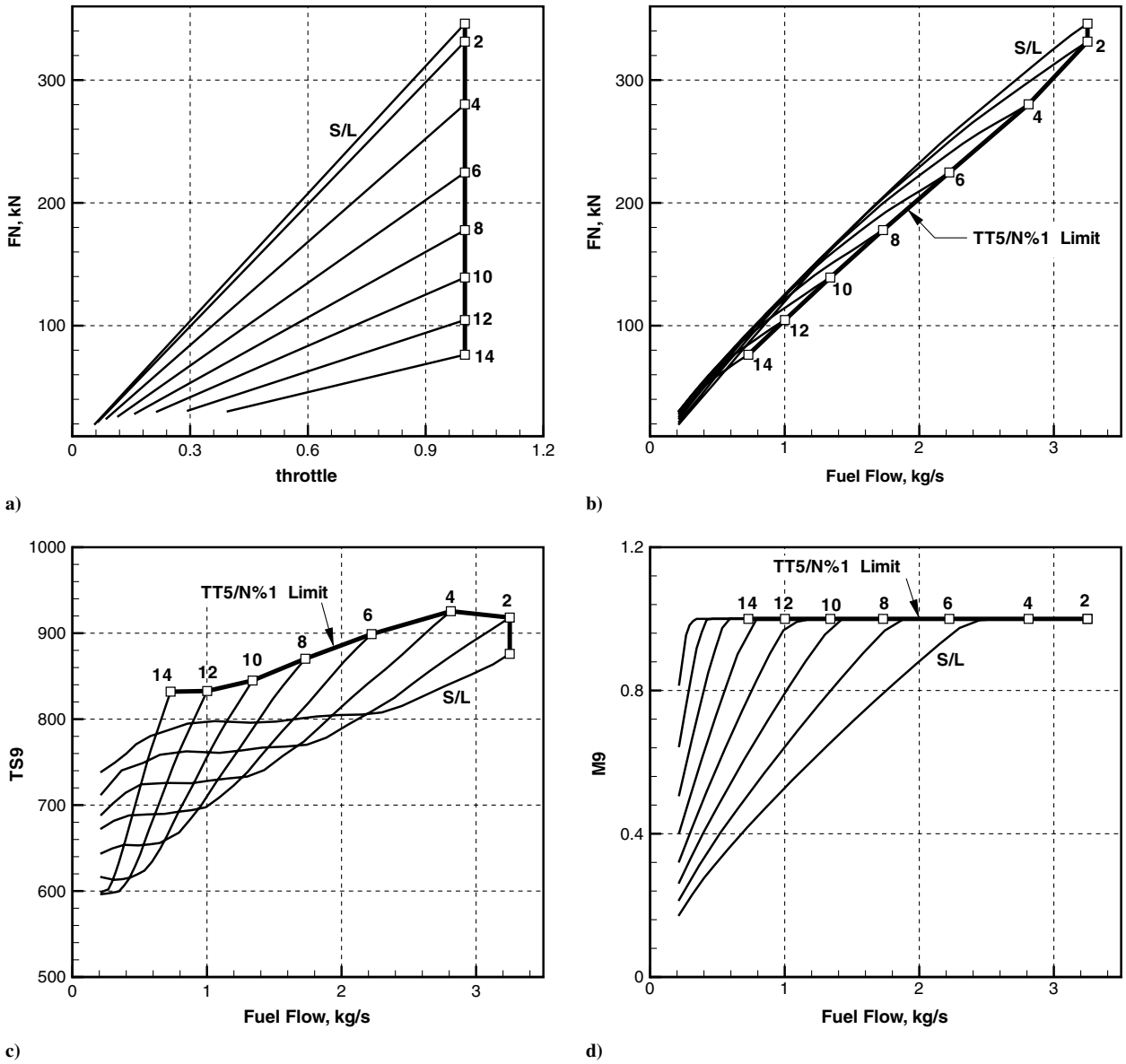

Fig. 12 Simulated engine performance for GP-7270 (selected parameters); *S/L* indicates sea level conditions.

recognized standards to present the data. For this airplane, the manufacturer claims a maximum structural payload (MSP) of 90,718 kg, while the unofficial performance charts[‡] are presented with a MSP = 83,700 kg. We have performed calculations with both values. We have made the following assumptions: 1) ISA, no wind, except at takeoff, which was −2 m/s (3.9 kt headwind); 2) holding time = 30 min, 3) diversion range = 200 nm, 4) diversion altitude = FCA − 2,000 ft, 5) 5% fuel reserve, 6) taxi-out time = 12 min, 7.) APU fuel flow = 250 kg/h (about 50% max load), 8) Climb thrust = 70% maximum continuous thrust, and 9) terminal area maneuver includes one *U*-turn at takeoff and one *U*-turn at landing (40 nm total).

The results of the present analysis are shown in Fig. 14. A number of facts can be gleaned from looking at the various operation points. The maximum-payload range is the same as the reference data, although it has been obtained at a larger payload. The maximum-fuel range is not dependent on the MSP, because the weight profile is dominated by the fuel load. The same occurs for the ferry range, which in both cases is equal to the performance claimed. All things considered, the result is extremely good. The difference in range at the maximum passenger load is considerable (550 nm), but the derivative dZFW/dx discussed earlier is equal to the reference data. This means that the integration between airframe and propulsion

Table 2 Wetted area summary for the Airbus A380-861

Item	A_{wet} [m^2]	%	Comments
Fuselage	1599.3	39.21	
Nose	286.6	6.83	
Center	803.8	19.71	corrected for root wing section
Aft	403.9	9.90	corrected for root tail section
Wing-body blend	105.0	2.57	included in central section
Wing	1484.0	36.38	corrected for flap racks
Wing tips	0.0	0.00	
Winglets	10.0	0.25	
Horizontal tail	352.8	8.65	
Vertical tail	237.5	5.83	
Nacelles	236.0	5.78	
Pylons	114.8	2.81	
Flap racks	44.2	1.08	
Total wetted area	4078.5		

[‡]Airbus: A380 Airplane Characteristics, Revision Jan. 31, 2008. See also Revision Oct. 1, 2009. We presume these documents are not official. The airplane specifications have been updated, but the charts are presented on the basis of an earlier airplane design.

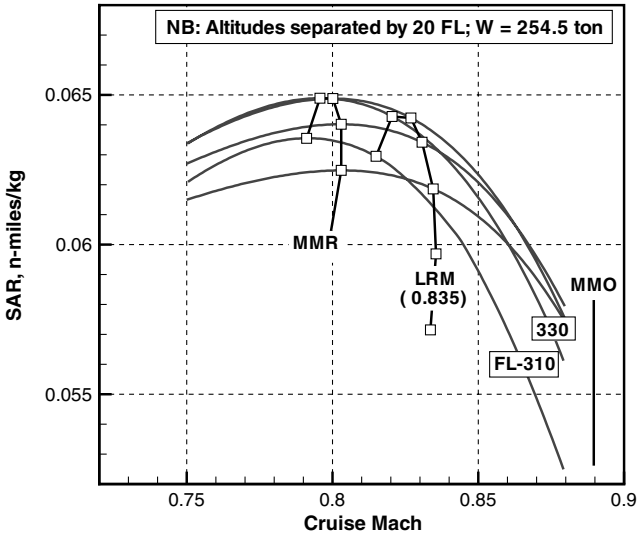

Fig. 13 Calculated SAR chart for the Boeing B-777-300-GE; standard day, no wind.

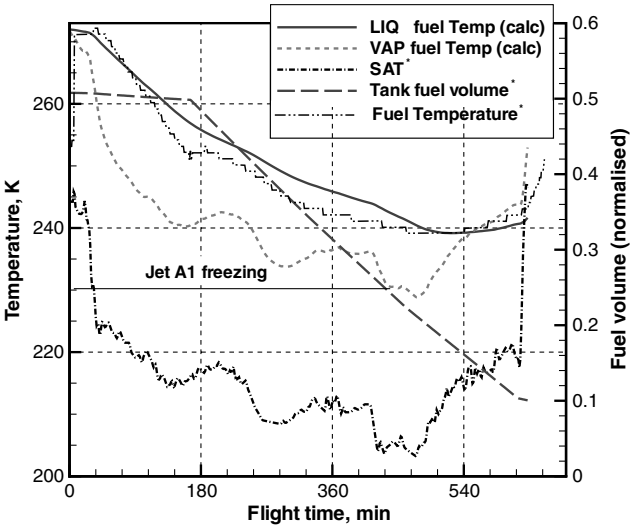

Fig. 15 Calculated wing tank fuel temperature compared with the data from the AAIB. [55]. Curves denoted with ( )* refer to FDR data.

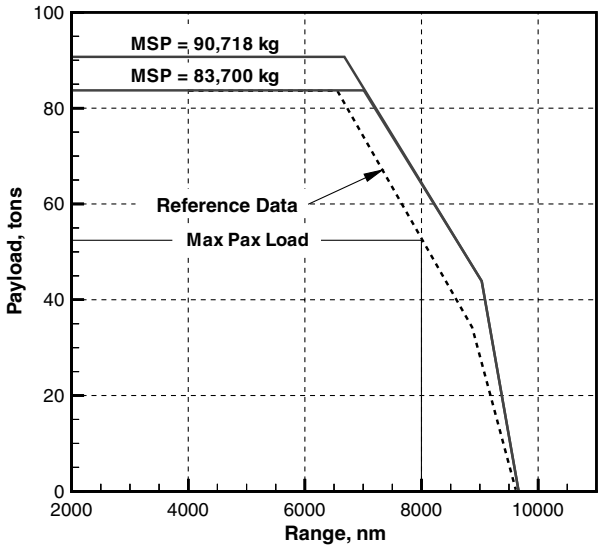

Fig. 14 Payload-range performance of the Airbus A380-861.

system is correct, and the engine performance data are not too far from the actual engine. Without further information on how the manufacturer's data have been determined and presented, there is no reason to attempt to improve our simulations. However, we are able to conclude that the prediction of the payload-range performance of an airplane cannot be done with simple methods, such as commonly used for preliminary design; these methods are never assessed in terms of accuracy, never validated, and hence intrinsically unreliable.

D. Thermophysics

An example of the fuel temperature analysis is shown in Fig. 15. The reference data, indicated by a star $(.)^*$ in the legend, are taken from an unofficial document of the UK Air Accident Investigation Branch (AAIB) for a well-publicized accident at London Heathrow Airport [55]. The reference data have been taken from the FDR. The figure displays the calculated fuel volume and the liquid fuel temperature during the flight. The high fuel rates during the climb cause the fuel level to go down faster (left side of the graph). The reference data are the recorded fuel temperature, the fuel use and the recorder total air temperature. The result is to be considered acceptable; any difference with the reference data can be attributed to several factors, including the accuracy of the tank geometry and the thermophysical properties of the fuel, which in most cases are inferred or interpolated. The fuel temperature itself is far from the freezing point. However, this particular case refers to an accident directly related to a combination of low fuel temperature and a systems failure in the fuel feed, where some freezing did occur. This test case further demonstrates that the use of FDR data is extremely valuable in such validation exercises.

Figure 16 shows some predicted AEO takeoff tire temperatures on the main and nose undercarriage units of the Boeing B-777-300, under the conditions described in the graph. A value of $\mathcal{H} = 0.12$ has been used, with a unique time step $\mathrm{d}t = 5 \cdot 10^{-2}$ s for both main and nose tires. Because of the difference in wheel diameter, a smaller time step would be required for the nose tires. A numerical study on the integration step proved that this detail was immaterial.

The rapid cooling after liftoff is due to the convection terms operating under the assumption of rotating wheels. The mechanical forcing of the tire ceases at liftoff; hence only cooling terms are left in the differential equations. The result is clearly sensitive to a large number of factors, including the position of the c.g. at takeoff (which determines the normal load distribution), on the tire inflation pressure, on the tire of inflation gas, on the structure of the tire itself and other parameters. The cooling effects are sensitive to the wheel rotation.

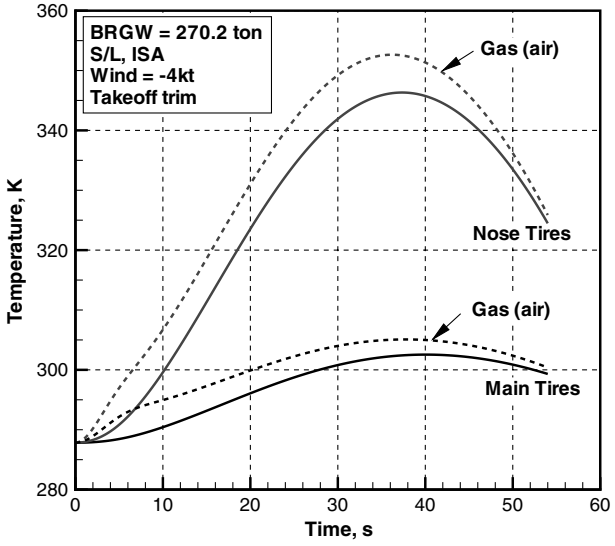

Fig. 16 Calculated average tire temperature for the Boeing B-777-300-GE; takeoff conditions.

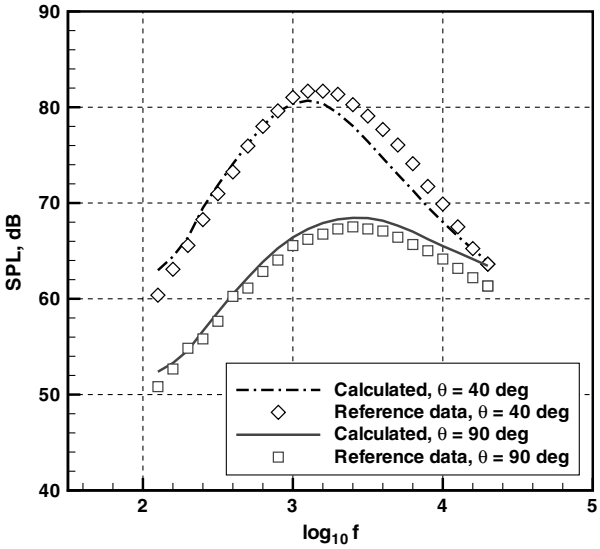

Fig. 17 Validation of coaxial jet noise; $\mathcal{T}_p = 800$ K, $V_p = 265$ m/s, $V_s = 170$ m/s. Reference data from interpolated from Fisher et al. [41].

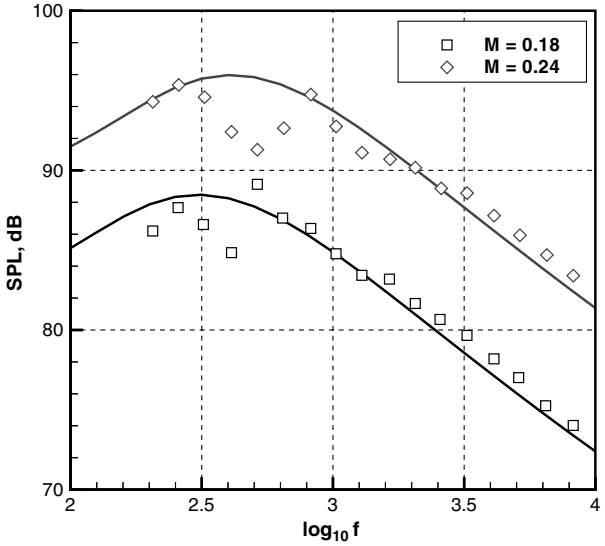

Fig. 18 Noise prediction of landing gear noise. Reference data interpolated from Guo [45].

No tire heating data have been found for takeoff conditions. Some data for typical taxi operations are given by Cavage [56] for the Boeing B-727, and taxi speeds up to 70 mph (110 km/h). The results indicate that the heating depends on the tire load, the taxi speed and the type of tire. A comparative analysis would be easy to carry out if the exact test conditions (c.g. position, load distribution, tire conditions and inflation pressure) were disclosed.

Data from Goodyear[§] indicate that the difference in temperature between tread center line and tread should negligible at normal taxi speeds. The temperature of the bead is higher at taxi speeds above 30 km/h, and may reach 30 K above the temperature of the tread. Thus, the method is only applicable to taxi conditions and normal takeoff procedures. In case of rejected takeoff, the results will only be approximate, because of the higher bead temperature.

E. Aircraft Noise

A case of noise validation at a component level is that of the engine jet, i.e., the nozzle in Fig. 4. Figure 17 shows a comparison between the predicted jet noise and test data extracted from Fisher et al. [40,41], for a case of a static coaxial nozzle, with specified parameters of the primary (core) and secondary (bypass) jets (indicated by underscore p and s, respectively). The core flow is a hot jet with a temperature $\mathcal{T}_p = 800$ K, a value comparable with the jet temperature in Fig. 12c. The polar emission angle θ is the angle between the jet axis and the line between the center of the nozzle and the receiver. Although this case does not refer specifically to a flight condition, the comparison is of acceptable accuracy, except at very low and very high frequencies.

Moving one step to determine the noise response of an airplane system, we show the main landing gear noise of the Boeing 737, whose reference data have been taken from [46]. A full breakdown of system components and relevant dimensions is given in the aforementioned paper. The noise measurements were taken on an isolated landing gear, with an array of microphones placed on a line 10 ft (3.05 m) from the center of the unit. The comparison between simulated noise and reference data is shown in Fig. 18 for 2 M numbers and polar emission angles equal to 90 deg. Again, this case does not refer to actual flight conditions. The comparison is acceptable in the full frequency spectrum, although the model's empirical parameters have been determined specifically for this landing gear geometry. The dip in SPL around 1 kHz is attributed to vortex shedding created by a link, that is not captured by the noise model.

[§]Manufacturers publish technical data to back-up performance claims; often these are not official reports.

IX. Conclusions

This paper has presented a simulation framework for modern transport airplanes. These airplanes must be considered as flight systems and modeled with interdisciplinary models for a full appreciation of their performance capability. Several theoretical models have been translated into a modular computer code `FLIGHT` that is demonstrated to be fully comprehensive. Whilst there can be limitations to the physics of each of the models, the software platform as a whole is representative of the complete aircraft. We envision the use of the platform for analyses such as direct operating costs, operational optimization at all levels (including trajectories), preliminary design, stability and control, aircraft certification, performance data verification, environmental analysis, noise trajectories, accident investigation and more. Because some of the models are built on top of the framework, they can be disconnected and used alongside other models for specific studies, such as aerodynamics and aircraft noise.

The paper has demonstrated that validation of an airplane model must follow a rational path, from the case of single physics on a single component, to multiphysics on the component, all the way to multiphysics to the complete system. However, we have never found a coherent set of reference data for a single airplane. To this date, there is a lack of data standards, and considerable opacity in most performance data, which should not be difficult to partially overcome if selected FDR recordings could be made available. Blind tests will remain a challenge for some time in the future.

We have explained that not always is it possible to extract the information required from the available technical literature. Therefore, some of the simplifications indicated earlier are necessary to have mathematical models that are robust enough to produce results of engineering relevance. When data are not available, they are inevitably inferred from a statistical analysis. Typical examples include the number of compressor blades, the nozzle/fan diameter ratio, etc. However, we emphasize that the core aspects of the model are based on first principles, rather than statistics.

Typically, a comprehensive model of the airplane, as presented in this paper includes: 1) a geometry model consisting of several hundred control points and rules for reconstruction; 2) a database of engine performance data containing no less than 20 engine parameters over the full flight envelope (generated with an engine model as part of the solution process; there is no reliance on manufacturer's data); 3) no less than 45 engine parameters (design limitations, dimensions, etc.); 4) no less than 40 airplane parameters (design limitations, key dimensions, etc.), and 5) no less than 40 operational parameters (atmospheric conditions at takeoff, cruise, landing; several operational requirements), along with a fair number

of ad-hoc parameters to supplement missing information (from tire material composition to the number of compressor blades, rotor-stator spacing, APU running mode, etc.). Because of these requirements, preliminary aircraft design is not possible. The domain of our computer program is within the specific niche of detailed aircraft performance analysis.

The run times required on a current dual-processor laptop or desktop computer, under common operating systems (Linux and Windows) are as follows: 2–6 min for a full mission analysis (the time depends on the aircraft range, the type of calculations required and the convergence tolerance). A noise trajectory requires about 30 s per receiver point. Most of the CPU used for noise calculations is attributed to the signal analysis. A payload-range chart may require up to 1 h; this effort can be reduced to about 10 m with less stringent convergence criteria.

Acknowledgment

Part of this work has been carried out under a European Commission Clean Sky grant SGO-03-002, project Flight-Noise (project code R-111664).

References

[1] Antoine, N. E., and Kroo, I., "A Framework for Aircraft Conceptual Design and Environmental Performance Studies," *AIAA Journal*, Vol. 43, No. 10, Oct. 2005, pp. 2100–2109. doi:10.2514/1.13017

[2] McCullers, L. A., "Aircraft Configuration Optimization Including Optimized Flight Profiles," *Experiences in Multidisciplinary Analysis and Optimization*, NASA CP-2327, Jan 1984, pp. 394–412.

[3] Filippone, A., "Comprehensive Analysis of Transport Aircraft Flight Performance," *Progress in Aerospace Sciences*, Vol. 44, No. 3, April 2007, pp. 192–236.

[4] Filippone, A., "Steep-Descent Manoeuvre of Transport Aircraft," *Journal of Aircraft*, Vol. 44, No. 5, Sept. 2007, pp. 1727–1739. doi:10.2514/1.28980

[5] Filippone, A., "Analysis of Carbon-Dioxide Emissions from Transport Aircraft," *Journal of Aircraft*, Vol. 45, No. 1, Jan. 2008, pp. 183–195.

[6] Visser, W. J. P., and Broomhead, M. J., "GSP: A Generic Object-Oriented Gas Turbine Simulation Environment," *ASME Gas Turbine Conference*, American Society of Mechanical Engineers Paper 2000-GT-0002, Munich, Germany, 2000.

[7] International Civil Aviation Organization, Engine Data Bank, Issue 15-B, Oct. 2007.

[8] Nielsen, J., *Missile Aerodynamics*, McGraw–Hill, New York, 1960, Chap. 9.

[9] Hopkins, E. J., "Charts for Predicting Turbulent Skin Friction from the Van Driest Method II," NASA, Technical Rept. TN-D-6945, Oct. 1972.

[10] Hopkins, E. J., and Inouye, M., "An Evaluation of Theories for Predicting Turbulent Skin Friction and Heat Transfer on Flat Plates at Supersonic and Hypersonic Mach Numbers," *AIAA Journal*, Vol. 9, No. 6, June 1971, pp. 993–1003. doi:10.2514/3.6323

[11] Blumer, C. B., and van Driest, E. R., "Boundary Layer Transition-Freestream Turbulence and Pressure Effects," *AIAA Journal*, Vol. 1, No. 6, 1963, pp. 1303–1306. doi:10.2514/3.1784

[12] Hoerner, S. F., *Fluid Dynamic Drag*, Hoerner, S. F., Bricktown, NJ, 1965.

[13] White, F., *Viscous Fluid Flow*, McGraw–Hill, New York, 1974, Chap. 7.

[14] Engineering Sciences Data Unit, "Drag Increment due to Fuselage Upsweep," Data Item 80006, ESDU International, London, Feb. 1988.

[15] Malone, B., and Mason, W. H., "Multidisciplinary Optimization in Aircraft Design Using Analytic Technology Models," *Journal of Aircraft*, Vol. 32, No. 2, March 1995, pp. 431–437. doi:10.2514/3.46734

[16] Engineering Sciences Data Unit, "Wing Lift Coefficient Increment at Zero Angle of Attack due to Deployment of Plain Trailing-Edge Flaps at Low Speeds," Data Item 97011, ESDU International, London, Nov. 2003.

[17] Engineering Sciences Data Unit, "Undercarriage Drag Prediction Methods," Data Item 79015, ESDU International, London, March 1987.

[18] *Proceedings of the 4th AIAA CFD Drag Prediction Workshop*, AIAA, Reston, VA, June 2009.

[19] Peng, D. Y., and Robinson, D. B., "A New Two-Constant Equation of State," *Industrial and Engineering Chemistry*, Vol. 15, No. 1, 1976, pp. 59–64. doi:10.1021/i360057a011

[20] Faith, L. E., Ackerman, G. H., and Henderson, H. T., "Heat Sink Capability of a Jet A Fuel: Heat Transfer and Coking Studies," NASA, Technical Rept. CR-72951, July 1971.

[21] Incropera, F., and De Witt, D. P., *Introduction to Heat Transfer*, John Wiley, New York, 1985, Chapt. 9.

[22] McAllen, J., Cuitino, A. M., and Sernas, V., "Numerical Investigation of the Deformation Characteristics and Heat Generation in Pneumatic Aircraft Tires. Part I: Mechanical Modeling," *Finite Elements in Analysis and Design*, Vol. 23, Nos. 2–4, 1996, pp. 241–263. doi:10.1016/S0168-874X(96)80010-2

[23] McAllen, J., Cuitino, A. M., and Sernas, V., "Numerical Investigation of the Deformation Characteristics and Heat Generation in Pneumatic Aircraft Tires, Part II: Thermal Modeling," *Finite Elements in Analysis and Design*, Vol. 23, Nos. 2–4, 1996, pp. 265–290. doi:10.1016/S0168-874X(96)80011-4

[24] Engineering Sciences Data Unit, "Vertical Deflection Characteristics of Aircraft Tyres," Data Item 86005, ESDU International, London, May 1986.

[25] Lin, Y. J., and Hwang, S. J., "Temperature Prediction or Rolling Tires by Computer Simulation," *Mathematics and Computers in Simulation*, Vol. 67, No. 3, 2004, pp. 235–249. doi:10.1016/j.matcom.2004.07.002

[26] Seghir–Ouali, S., Saury, D., Harmand, S., Phillipart, P., and Laloy, O., "Convective Heat Transfer Inside a Rotating Cylinder with an Axial Flow," *International Journal of Thermal Sciences*, Vol. 45, No. 11, 2006, pp. 1066–1078. doi:10.1016/j.ijthermalsci.2006.02.001

[27] McCarty, J. L., and Tanner, J. A., "Temperature Distribution in an Aircraft Tire at Low Ground Speeds," NASA, Technical Rept. TP-2195, 1983.

[28] Engineering Sciences Data Unit, "Frictional and Retarding Forces on Aircraft Tyres, Part IV: Estimation of Effects of Yaw," Data item 86016, ESDU International, London, Oct. 1992.

[29] Dreher, R. C., and Tanner, J. A., "Experimental Investigation of the Braking and Cornering Characteristics of 3011.5 × 14.5 Type VIII: Aircraft Tires with Different Tread Patterns," NASA, Technical Rept. TN D-7743, Oct. 1974.

[30] Engineering Sciences Data Unit, "Calculation of Ground Performance in Takeoff and Landing," Data Item 85029, ESDU International, London, March 2006.

[31] Engineering Sciences Data Unit, "Force and Moment Components in Takeoff and Landing Calculations," Data Item 85030, ESDU International, London, Nov. 1985.

[32] Engineering Sciences Data Unit, "Frictional and Retarding Forces on Aircraft Tyres. Part II: Estimation of Braking Force," Data Item 88023, ESDU International, London, June 1995.

[33] Torenbeek, E., "Cruise Performance and Range Prediction Reconsidered," *Progress in Aerospace Sciences*, Vol. 33, Nos. 5–6, May–June 1997, pp. 285–321. doi:10.1016/S0376-0421(96)00007-3

[34] Press, W. H., Teukolsky, S. A., Vetterling, W. T., and Flannery, B. P., *Numerical Recipes*, Cambridge Univ. Press, Cambridge, England, 3rd ed., 2000.

[35] Smith, M. T. J., *Aircraft Noise*, Cambridge Univ. Press, Cambridge, England, 1989.

[36] Fink, M. R., "Noise Component Method for Airframe Noise," *Journal of Aircraft*, Vol. 16, No. 10, 1979, pp. 659–665. doi:10.2514/3.58586

[37] Fink, M. R., and Schlinke, R. H., "Airframe Noise Component Interaction Studies," *Journal of Aircraft*, Vol. 17, No. 2, 1980, pp. 99–105. doi:10.2514/3.57880

[38] Heidmann, M. F., "Interim Prediction Method for Fan and Compressor Noise Source," NASA, Technical Rept. TM X-71763, 1975.

[39] ESDU, "Prediction of Combustor Noise from Gas Turbine Engines," Data Item 05001, ESDU International, London, Feb. 2005.

[40] Fisher, M. J., Preston, G. A., and Bryce, W. D., "A Modelling of the Noise from Coaxial Jets. Part 1: With Unheated Primary Flow," *Journal of Sound and Vibration*, Vol. 209, No. 3, Jan. 1998, pp. 385–403. doi:10.1006/jsvi.1997.1218

[41] Fisher, M. J., Preston, G. A., and Mead, W. D., "A Modelling of the

Noise from Coaxial Jets. Part 2: With Heated Primary Flow," *Journal of Sound and Vibration*, Vol. 209, No. 3, Jan. 1998, pp. 405–417. doi:10.1006/jsvi.1997.1217

[42] Gerhold, C. H., "Analytical Model of Jet Shielding," *AIAA Journal*, Vol. 21, No. 5, May 1983, pp. 694–698. doi:10.2514/3.8135

[43] Simonich, J. C., Amiet, R. K., and Schlinker, R. H., "Jet Shielding of Jet Noise," NASA, Technical Rept. CR-3966, 1986.

[44] Engineering Sciences Data Unit, "Jet-by-Jet Shielding of Noise," Data Item 88023, ESDU International, London, March 1992.

[45] Guo, Y. P., "Empirical Prediction of Aircraft Landing Gear Noise," NASA, Technical Rept. CR-2005-213780, 2005.

[46] Guo, Y. P., Yamamoto, K. J., and Stoker, R. W., "Experimental Study on Aircraft Landing Gear Noise," *Journal of Aircraft*, Vol. 43, No. 2, March 2006, pp. 306–317. doi:10.2514/1.11085

[47] Guo, Y. P., Yamamoto, K. J., and Stoker, R. W., "Component-Based Empirical Model for High Lift System Noise Prediction," *Journal of Aircraft*, Vol. 40, No. 5, Sept. 2003, pp. 914–922. doi:10.2514/2.6867

[48] Lilley, G. M., "The Prediction of Airframe Noise and Comparison with Experiment," *Journal of Sound and Vibration*, Vol. 239, No. 4, 2001, pp. 849–859. doi:10.1006/jsvi.2000.3219

[49] Brooks, T. F., and Humphreys, W. M., "Flap-Edge Aeroacoustic Measurements and Predictions," *Journal of Sound and Vibration*, Vol. 261, No. 1, 2003, pp. 31–74. doi:10.1016/S0022-460X(02)00939-2

[50] Engineering Sciences Data Unit, "Airframe Noise Prediction," Data Item 90023, ESDU International, London, June 2003.

[51] ISO, "Attenuation of Sound During Propagation Outdoors, Part I: Calculation of the Absorption of Sound by the Atmosphere," International Standards Organization, Technical Rept. ISO-9613-1, Geneve, CH, 1993.

[52] Attenborough, K., "Ground Parameter Information for Propagation Modeling," *Journal of the Acoustical Society of America*, Vol. 92, No. 1, Jan 1992, pp. 418–427. doi:10.1121/1.404251

[53] Engineering Sciences Data Unit, "The Correction of Measured Noise Spectra for the Effects of Ground Reflection," Data Item 94035, ESDU International, London, Dec. 1994.

[54] Guo, Y. P., "A Component-Based Model for Aircraft Landing Gear Noise Prediction," *Journal of Sound and Vibration*, Vol. 312, Nos. 4–5, 2008, pp. 801–820.

[55] Air Accidents Investigation Board, "Accident to Boeing B-777-236ER, G-YMMM at London Heathrow Airport on 17 January 2007," Interim Rept. EW/C2008/01, Aldershot, Hants, UK, Sept. 2008.

[56] Cavage, W. M., "Heating Comparison of Radial and Bias-Ply Tires on a B-727 Aircraft," U.S. Dept. of Transportation, Technical Rept. DOT/FAA/AR-TN97/50, Nov. 1997.